

## DIII-D RESEARCH ADVANCING THE PHYSICS BASIS FOR OPTIMIZING THE TOKAMAK APPROACH TO FUSION ENERGY

M. Fenstermacher for the DIII-D Team<sup>1</sup>, J. Abbate<sup>2</sup>, S. Abe<sup>3</sup>, T. Abrams<sup>4</sup>, M. Adams<sup>4</sup>, B. Adamson<sup>4</sup>, N. Aiba<sup>5</sup>, T. Akiyama<sup>4</sup>, P. Aleynikov<sup>6</sup>, E. Allen<sup>4</sup>, S. Allen<sup>1</sup>, H. Anand<sup>4</sup>, J. Anderson<sup>4</sup>, Y. Andrew<sup>7</sup>, T. Andrews<sup>4</sup>, D. Appelt<sup>4</sup>, R. Arbon<sup>3</sup>, N. Ashikawa<sup>8</sup>, A. Ashourvan<sup>2</sup>, M. Aslin<sup>9</sup>, Y. Asnis<sup>10</sup>, M. Austin<sup>11</sup>, D. Ayala<sup>4</sup>, J. Bak<sup>12</sup>, I. Bandyopadhyay<sup>13</sup>, S. Banerjee<sup>14</sup>, K. Barada<sup>15</sup>, L. Bardoczi<sup>4</sup>, J. Barr<sup>4</sup>, E. Bass<sup>16</sup>, D. Battaglia<sup>2</sup>, A. Battey<sup>17</sup>, W. Baumgartner<sup>18</sup>, L. Baylor<sup>19</sup>, J. Beckers<sup>20</sup>, M. Beidler<sup>19</sup>, E. Belli<sup>4</sup>, J. Berkery<sup>17</sup>, T. Bernard<sup>21</sup>, N. Bertelli<sup>2</sup>, M. Beurskens<sup>6</sup>, R. Bielajew<sup>18</sup>, S. Bilgili<sup>22</sup>, B. Biswas<sup>18</sup>, S. Blondel<sup>23</sup>, J. Boedo<sup>16</sup>, I. Bogatu<sup>24</sup>, R. Boivin<sup>4</sup>, T. Bolzonella<sup>25</sup>, M. Bongard<sup>26</sup>, X. Bonnin<sup>27</sup>, P. Bonoli<sup>18</sup>, M. Bonotto<sup>25</sup>, A. Bortolon<sup>2</sup>, S. Bose<sup>3</sup>, N. Bosviel<sup>28</sup>, S. Bouwmans<sup>20</sup>, M. Boyer<sup>2</sup>, W. Boyes<sup>17</sup>, L. Bradley<sup>15</sup>, R. Brambila<sup>4</sup>, D. Brennan<sup>3</sup>, S. Bringuier<sup>4</sup>, L. Brodsky<sup>4</sup>, M. Brookman<sup>4</sup>, J. Brooks<sup>29</sup>, D. Brower<sup>15</sup>, G. Brown<sup>1</sup>, W. Brown<sup>2</sup>, M. Burke<sup>26</sup>, K. Burrell<sup>4</sup>, K. Butler<sup>23</sup>, R. Buttery<sup>4</sup>, I. Bykov<sup>16</sup>, P. Byrne<sup>4</sup>, A. Cacheris<sup>23</sup>, K. Callahan<sup>15</sup>, J. Callen<sup>26</sup>, G. Campbell<sup>4</sup>, J. Candy<sup>4</sup>, J. Canik<sup>19</sup>, P. Cano-Megias<sup>30</sup>, N. Cao<sup>18</sup>, L. Carayannopoulos<sup>18</sup>, T. Carlstrom<sup>4</sup>, W. Carrig<sup>4</sup>, T. Carter<sup>15</sup>, W. Cary<sup>4</sup>, L. Casali<sup>4</sup>, M. Cengher<sup>4</sup>, G. Cespedes Paz<sup>31</sup>, R. Chaban<sup>32</sup>, V. Chan, B. Chapman<sup>26</sup>, I. Char<sup>33</sup>, A. Chattopadhyay<sup>34</sup>, R. Chen<sup>35</sup>, J. Chen<sup>35</sup>, X. Chen<sup>4</sup>, X. Chen<sup>18</sup>, J. Chen<sup>36</sup>, M. Chen<sup>37</sup>, J. Chen<sup>15</sup>, Z. Chen<sup>11</sup>, M. Choi<sup>12</sup>, W. Choi<sup>3</sup>, G. Choi<sup>38</sup>, L. Chousal<sup>16</sup>, C. Chrobak<sup>39</sup>, C. Chrystal<sup>4</sup>, Y. Chung<sup>33</sup>, R. Churchill<sup>12</sup>, M. Cianciosa<sup>19</sup>, J. Clark<sup>40</sup>, M. Clement<sup>2</sup>, S. Coda<sup>41</sup>, A. Cole<sup>42</sup>, C. Collins<sup>19</sup>, W. Conlin<sup>3</sup>, A. Cooper<sup>41</sup>, J. Cordell<sup>2</sup>, B. Coriton<sup>4</sup>, T. Cote<sup>26</sup>, J. Cothran<sup>43</sup>, A. Creely<sup>18</sup>, N. Crocker<sup>15</sup>, C. Crowe<sup>4</sup>, B. Crowley<sup>4</sup>, T. Crowley<sup>44</sup>, D. Cruz-Zabala<sup>30</sup>, D. Cummings<sup>4</sup>, M. Curie<sup>11</sup>, D. Curreli<sup>45</sup>, A. Dal Molin<sup>46</sup>, B. Dannels<sup>19</sup>, A. Dautt-Silva<sup>4</sup>, K. Davda<sup>23</sup>, G. De Tommasi<sup>47</sup>, P. De Vries<sup>27</sup>, G. Degrandchamp<sup>38</sup>, J. Degraessie<sup>4</sup>, D. Demers<sup>44</sup>, S. Denk<sup>18</sup>, S. Depasquale<sup>2</sup>, E. Deshazer<sup>48</sup>, A. Diallo<sup>2</sup>, S. Diem<sup>26</sup>, A. Dimits<sup>1</sup>, R. Ding<sup>35</sup>, S. Ding<sup>21</sup>, W. Ding<sup>15</sup>, T. Do<sup>16</sup>, J. Doane<sup>4</sup>, G. Dong<sup>2</sup>, D. Donovan<sup>23</sup>, J. Drake<sup>4</sup>, W. Drews<sup>4</sup>, J. Drobný<sup>45</sup>, X. Du<sup>4</sup>, H. Du<sup>49</sup>, V. Duarte<sup>2</sup>, D. Dudt<sup>3</sup>, C. Dunn<sup>48</sup>, J. Duran<sup>23</sup>, A. Dvorak<sup>19</sup>, F. Effenberg<sup>2</sup>, N. Eidietis<sup>4</sup>, D. Elder<sup>50</sup>, D. Eldon<sup>4</sup>, R. Ellis<sup>2</sup>, W. Elwasif<sup>19</sup>, D. Ennis<sup>51</sup>, K. Erickson<sup>2</sup>, D. Ernst<sup>18</sup>, M. Fasciana<sup>52</sup>, D. Fedorov<sup>21</sup>, E. Feibush<sup>2</sup>, N. Ferraro<sup>2</sup>, J. Ferreira<sup>53</sup>, J. Ferron<sup>4</sup>, P. Fimognari<sup>44</sup>, D. Finkenthal<sup>54</sup>, R. Fitzpatrick<sup>11</sup>, P. Fox<sup>55</sup>, W. Fox<sup>2</sup>, L. Frassinetti<sup>56</sup>, H. Frerichs<sup>26</sup>, H. Frye<sup>57</sup>, Y. Fu<sup>3</sup>, K. Gage<sup>38</sup>, J. Galdon Quiroga<sup>6</sup>, A. Gallo<sup>21</sup>, Q. Gao<sup>49</sup>, A. Garcia<sup>38</sup>, M. Garcia Munoz<sup>30</sup>, D. Garnier<sup>18</sup>, A. Garofalo<sup>4</sup>, A. Gattuso<sup>4</sup>, D. Geng<sup>4</sup>, K. Gentle<sup>11</sup>, D. Ghosh<sup>1</sup>, L. Giacomelli<sup>58</sup>, S. Gibson<sup>59</sup>, E. Gilson<sup>2</sup>, C. Giroud<sup>55</sup>, F. Glass<sup>4</sup>, A. Glasser<sup>3</sup>, D. Glibert<sup>4</sup>, P. Gohil<sup>4</sup>, R. Gomez<sup>4</sup>, S. Gomez<sup>4</sup>, X. Gong<sup>35</sup>, E. Gonzales<sup>4</sup>, A. Goodman<sup>3</sup>, Y. Gorelov<sup>4</sup>, V. Graber<sup>60</sup>, R. Granetz<sup>18</sup>, T. Gray<sup>19</sup>, D. Green<sup>19</sup>, C. Greenfield<sup>4</sup>, M. Greenwald<sup>18</sup>, B. Grierson<sup>2</sup>, R. Groebner<sup>4</sup>, W. Grosnickle<sup>4</sup>, M. Groth<sup>61</sup>, H. Grunloh<sup>4</sup>, S. Gu<sup>21</sup>, W. Guo<sup>35</sup>, H. Guo<sup>4</sup>, P. Gupta<sup>4</sup>, J. Guterl<sup>4</sup>, W. Guttenfelder<sup>2</sup>, T. Guzman<sup>4</sup>, S. Haar<sup>4</sup>, R. Hager<sup>2</sup>, S. Hahn<sup>12</sup>, M. Halfmoon<sup>11</sup>, T. Hall<sup>4</sup>, K. Hallatschek<sup>6</sup>, F. Halpern<sup>4</sup>, G. Hammett<sup>2</sup>, H. Han<sup>62</sup>, E. Hansen<sup>38</sup>, C. Hansen<sup>63</sup>, M. Hansink<sup>4</sup>, J. Hanson<sup>17</sup>, M. Hanson<sup>16</sup>, G. Hao<sup>49</sup>, A. Harris<sup>4</sup>, R. Harvey<sup>64</sup>, S. Haskey<sup>2</sup>, E. Hassan<sup>11</sup>, A. Hassanein<sup>29</sup>, D. Hatch<sup>11</sup>, R. Hawryluk<sup>2</sup>, W. Hayashi<sup>38</sup>, W. Heidbrink<sup>38</sup>, J. Herfindal<sup>19</sup>, J. Hicok<sup>4</sup>, D. Hill<sup>4</sup>, E. Hinson<sup>26</sup>, C. Holcomb<sup>1</sup>, L. Holland<sup>4</sup>, C. Holland<sup>16</sup>, E. Hollmann<sup>16</sup>, J. Hollocombe<sup>55</sup>, A. Holm<sup>61</sup>, I. Holmes<sup>4</sup>, K. Holtrop<sup>4</sup>, M. Honda<sup>5</sup>, R. Hong<sup>15</sup>, R. Hood<sup>65</sup>, A. Horton<sup>19</sup>, L. Horvath<sup>55</sup>, M. Hosokawa<sup>27</sup>, S. Houshmandyar<sup>11</sup>, N. Howard<sup>18</sup>, E. Howell<sup>66</sup>, D. Hoyt<sup>4</sup>, W. Hu<sup>35</sup>, Y. Hu<sup>35</sup>, Q. Hu<sup>2</sup>, J. Huang<sup>35</sup>, Y. Huang<sup>35</sup>, J. Hughes<sup>18</sup>, T. Human<sup>2</sup>, D. Humphreys<sup>4</sup>, P. Huynh<sup>4</sup>, A. Hyatt<sup>4</sup>, C. Ibanez<sup>4</sup>, L. Ibarra<sup>4</sup>, R. Icasas<sup>4</sup>, K. Ida<sup>8</sup>, V. Igochine<sup>6</sup>, Y. In<sup>67</sup>, S. Inoue<sup>5</sup>, A. Isayama<sup>5</sup>, O. Izacard<sup>3</sup>, V. Izzo<sup>4</sup>, A. Jackson<sup>55</sup>, G. Jacobsen<sup>4</sup>, A. Jaervinen<sup>61</sup>, A. Jalalvand<sup>68</sup>, J. Janhunen<sup>11</sup>, S. Jardin<sup>2</sup>, H. Jarleblad<sup>69</sup>, Y. Jeon<sup>12</sup>, H. Ji<sup>3</sup>, X. Jian<sup>16</sup>, E. Joffrin<sup>70</sup>, A. Johansen<sup>63</sup>, C. Johnson<sup>51</sup>, T. Johnson<sup>71</sup>, C. Jones<sup>16</sup>, I. Joseph<sup>1</sup>, D. Jubas<sup>3</sup>, B. Junge<sup>4</sup>, W. Kalb<sup>18</sup>, R. Kalling<sup>72</sup>, C. Kamath<sup>1</sup>, J. Kang<sup>12</sup>, D. Kaplan<sup>4</sup>, A. Kaptanoglu<sup>63</sup>, S. Kasdorf<sup>73</sup>, J. Kates-Harbeck<sup>74</sup>, P. Kazantzidis<sup>75</sup>, A. Kellman<sup>4</sup>, D. Kellman<sup>4</sup>, C. Kessel<sup>19</sup>, K. Khumthong<sup>4</sup>, E. Kim<sup>76</sup>, H. Kim<sup>77</sup>, J. Kim<sup>24</sup>, S. Kim<sup>27</sup>, J. Kim<sup>12</sup>, H. Kim<sup>12</sup>, K. Kim<sup>19</sup>, C. Kim<sup>78</sup>, W. Kimura<sup>79</sup>, M. King<sup>4</sup>, J. King<sup>66</sup>, J. Kinsey<sup>64</sup>, A. Kirk<sup>55</sup>, B. Kiyan<sup>3</sup>, A. Kleiner<sup>2</sup>, V. Klevarova<sup>68</sup>, R. Knapp<sup>4</sup>, M. Knolker<sup>21</sup>, W. Ko<sup>12</sup>, T. Kobayashi<sup>8</sup>, E. Koch<sup>4</sup>, M. Kochan<sup>55</sup>, B. Koel<sup>3</sup>, M. Koepke<sup>22</sup>, A. Kohn<sup>80</sup>, R. Kolasinski<sup>65</sup>, E. Kolen<sup>2</sup>, E. Kostadinova<sup>81</sup>, M. Kostuk<sup>4</sup>, G. Kramer<sup>2</sup>, D. Kriete<sup>26</sup>, L. Kripner<sup>82</sup>, S. Kubota<sup>15</sup>, J. Kulchar<sup>4</sup>, K. Kwon<sup>67</sup>, R. La Haye<sup>4</sup>, F. Laggner<sup>2</sup>, H. Lan<sup>35</sup>, R. Lantsov<sup>15</sup>, L. Lao<sup>4</sup>, A. Lasa Esquisabel<sup>23</sup>, C. Lasnier<sup>1</sup>, C. Lau<sup>19</sup>, B. Leard<sup>60</sup>, J. Lee<sup>83</sup>, R. Lee<sup>4</sup>, M. Lee<sup>84</sup>, M. Lee<sup>12</sup>, Y. Lee<sup>12</sup>, C. Lee<sup>85</sup>, J. Lee<sup>85</sup>, S. Lee<sup>23</sup>, M. Lehen<sup>27</sup>, A. Leonard<sup>4</sup>, E. Leppink<sup>18</sup>, M. Leshner<sup>4</sup>, J. Lestz<sup>38</sup>, J. Leuer<sup>4</sup>, N. Leuthold<sup>6</sup>, X. Li<sup>35</sup>, K. Li<sup>35</sup>, E. Li<sup>35</sup>, G. Li<sup>35</sup>, L. Li<sup>86</sup>, Z. Li<sup>21</sup>, J. Li<sup>49</sup>, Y. Li<sup>87</sup>, Z. Lin<sup>38</sup>, D. Lin<sup>38</sup>, X. Liu<sup>35</sup>, J. Liu<sup>35</sup>, Y. Liu<sup>35</sup>, T. Liu<sup>88</sup>, Y. Liu<sup>4</sup>, C. Liu<sup>4</sup>, Z. Liu<sup>48</sup>, C. Liu<sup>2</sup>, D. Liu<sup>3</sup>, A. Liu<sup>3</sup>, D. Liu<sup>38</sup>, A. Loarte-Prieto<sup>27</sup>, L. Lodestro<sup>1</sup>, N. Logan<sup>1</sup>, J. Lohr<sup>4</sup>, B. Lombardo<sup>4</sup>, J. Lore<sup>19</sup>, Q. Luan<sup>88</sup>, T. Luce<sup>27</sup>, T. Luda Di Cortemiglia<sup>6</sup>, N. Luhmann<sup>37</sup>, R. Lunsford<sup>2</sup>, Z. Luo<sup>35</sup>, A. Lvovskiy<sup>4</sup>, B. Lyons<sup>4</sup>, X. Ma<sup>21</sup>, M. Madruga<sup>4</sup>, B. Madsen<sup>69</sup>, C. Maggi<sup>55</sup>, K. Maheshwari<sup>89</sup>, A. Mail<sup>4</sup>, J. Mailloux<sup>55</sup>, R. Maingi<sup>2</sup>, M. Major<sup>26</sup>, M. Makowski<sup>90</sup>, R. Manchanda<sup>34</sup>, C. Marini<sup>21</sup>, A. Marinoni<sup>18</sup>, A. Maris<sup>18</sup>, T. Markovic<sup>82</sup>, L. Marrelli<sup>25</sup>, E. Martin<sup>19</sup>, J. Mateja<sup>29</sup>, G. Matsunaga<sup>5</sup>, R. Maurizio<sup>21</sup>, P. Mauzey<sup>4</sup>, D. Mauzey<sup>2</sup>, G. Mcardle<sup>55</sup>, J. McClenaghan<sup>4</sup>, K. Mccollam<sup>26</sup>, C. Mcdevitt<sup>91</sup>, K. Mckay<sup>14</sup>, G. Mckee<sup>26</sup>, A. Mclean<sup>1</sup>, V. Mehta<sup>33</sup>, E. Meier<sup>92</sup>, J. Menard<sup>2</sup>, O. Meneghini<sup>4</sup>, G. Merlo<sup>11</sup>, S. Messer<sup>23</sup>, W. Meyer<sup>1</sup>, C. Michael<sup>15</sup>, C. Michoski<sup>93</sup>,

P. Milne<sup>94</sup>, G. Minet<sup>4</sup>, A. Mischel<sup>2</sup>, Y. Mitrishkin<sup>95</sup>, C. Moeller<sup>4</sup>, K. Montes<sup>18</sup>, M. Morales<sup>96</sup>, S. Mordijck<sup>32</sup>, D. Moreau<sup>70</sup>, S. Morosohk<sup>60</sup>, P. Morris<sup>4</sup>, L. Morton<sup>26</sup>, A. Moser<sup>4</sup>, R. Moyer<sup>16</sup>, C. Moynihan<sup>45</sup>, T. Mrazkova<sup>97</sup>, D. Mueller<sup>2</sup>, S. Munaretto<sup>4</sup>, J. Munoz Burgos<sup>98</sup>, C. Murphy<sup>4</sup>, K. Murphy<sup>99</sup>, C. Muscatello<sup>4</sup>, C. Myers<sup>65</sup>, A. Nagy<sup>2</sup>, G. Nandipati<sup>100</sup>, M. Navarro<sup>26</sup>, F. Nave<sup>53</sup>, G. Navratil<sup>17</sup>, R. Nazikian<sup>2</sup>, A. Neff<sup>101</sup>, G. Neilson<sup>2</sup>, T. Neiser<sup>21</sup>, W. Neiswanger<sup>33</sup>, D. Nelson<sup>4</sup>, A. Nelson<sup>3</sup>, F. Nespoli<sup>2</sup>, R. Nguyen<sup>4</sup>, L. Nguyen<sup>102</sup>, X. Nguyen<sup>15</sup>, J. Nichols<sup>23</sup>, M. Nocente<sup>46</sup>, S. Nogami<sup>22</sup>, S. Noraky<sup>4</sup>, N. Norausky<sup>4</sup>, M. Nornberg<sup>26</sup>, R. Nygren<sup>65</sup>, T. Odstrcil<sup>4</sup>, D. Ogas<sup>4</sup>, T. Ogorman<sup>4</sup>, S. Ohdachi<sup>8</sup>, Y. Ohtani<sup>5</sup>, M. Okabayashi<sup>2</sup>, M. Okamoto<sup>103</sup>, L. Olavson<sup>104</sup>, E. Olofsson<sup>4</sup>, M. Omullane<sup>105</sup>, R. Oneill<sup>4</sup>, D. Orlov<sup>16</sup>, W. Orvis<sup>1</sup>, T. Osborne<sup>4</sup>, D. Pace<sup>4</sup>, G. Paganini Canal<sup>10</sup>, A. Pajares Martinez<sup>60</sup>, L. Palacios<sup>2</sup>, C. Pan<sup>35</sup>, Q. Pan<sup>18</sup>, R. Pandit<sup>14</sup>, M. Pandya<sup>26</sup>, A. Pankin<sup>2</sup>, Y. Park<sup>17</sup>, J. Park<sup>19</sup>, J. Park<sup>2</sup>, S. Parker<sup>73</sup>, P. Parks<sup>4</sup>, M. Parsons<sup>106</sup>, B. Patel<sup>87</sup>, C. Pawley<sup>4</sup>, C. Paz-Soldan<sup>4</sup>, W. Peebles<sup>15</sup>, S. Pelton<sup>21</sup>, R. Perillo<sup>16</sup>, C. Petty<sup>4</sup>, Y. Peysson<sup>70</sup>, D. Pierce<sup>4</sup>, A. Pigarov<sup>64</sup>, L. Pigatto<sup>25</sup>, D. Piglowski<sup>4</sup>, S. Pinches<sup>27</sup>, R. Pinsker<sup>4</sup>, P. Piovesan<sup>25</sup>, N. Piper<sup>48</sup>, A. Pironti<sup>47</sup>, R. Pitts<sup>27</sup>, J. Pizzo<sup>107</sup>, U. Plank<sup>6</sup>, M. Podesta<sup>2</sup>, E. Poli<sup>6</sup>, F. Poli<sup>2</sup>, D. Ponce<sup>4</sup>, Z. Popovic<sup>16</sup>, M. Porkolab<sup>18</sup>, G. Porter<sup>90</sup>, C. Powers<sup>108</sup>, S. Powers<sup>108</sup>, R. Prater<sup>4</sup>, Q. Pratt<sup>15</sup>, I. Pusztai<sup>109</sup>, J. Qian<sup>35</sup>, X. Qin<sup>26</sup>, O. Ra<sup>67</sup>, T. Rafiq<sup>60</sup>, T. Raines<sup>2</sup>, R. Raman<sup>63</sup>, J. Rauch<sup>4</sup>, A. Raymond<sup>4</sup>, C. Rea<sup>18</sup>, M. Reich<sup>6</sup>, A. Reiman<sup>2</sup>, S. Reinhold<sup>4</sup>, M. Reinke<sup>19</sup>, R. Reksoatmodjo<sup>14</sup>, Q. Ren<sup>35</sup>, Y. Ren<sup>2</sup>, J. Ren<sup>23</sup>, M. Rensink<sup>1</sup>, J. Renteria<sup>4</sup>, T. Rhodes<sup>15</sup>, J. Rice<sup>18</sup>, R. Roberts<sup>4</sup>, J. Robinson<sup>110</sup>, P. Rodriguez Fernandez<sup>18</sup>, T. Rognlien<sup>1</sup>, A. Rosenthal<sup>4</sup>, S. Rosiello<sup>111</sup>, J. Rost<sup>18</sup>, J. Roveto<sup>48</sup>, W. Rowan<sup>11</sup>, R. Rozenblat<sup>2</sup>, J. Ruane<sup>4</sup>, D. Rudakov<sup>16</sup>, J. Ruiz Ruiz<sup>112</sup>, R. Rupani<sup>4</sup>, S. Saarelma<sup>4</sup>, S. Sabbagh<sup>17</sup>, J. Sachdev<sup>2</sup>, J. Saenz<sup>4</sup>, S. Saib<sup>89</sup>, M. Salewski<sup>69</sup>, A. Salmi<sup>113</sup>, B. Sammulu<sup>4</sup>, C. Samuel<sup>1</sup>, A. Sandorfi<sup>114</sup>, C. Sang<sup>88</sup>, J. Sarff<sup>26</sup>, O. Sauter<sup>41</sup>, K. Schaubel<sup>4</sup>, L. Schmitz<sup>15</sup>, O. Schmitz<sup>26</sup>, J. Schneider<sup>33</sup>, P. Schroeder<sup>4</sup>, K. Schultz<sup>4</sup>, E. Schuster<sup>60</sup>, J. Schwartz<sup>3</sup>, F. Sciortino<sup>18</sup>, F. Scotti<sup>1</sup>, J. Scoville<sup>4</sup>, A. Seltzman<sup>18</sup>, S. Seol<sup>107</sup>, I. Sfiligoi<sup>16</sup>, M. Shafer<sup>19</sup>, S. Sharapov<sup>55</sup>, H. Shen<sup>4</sup>, Z. Sheng<sup>35</sup>, T. Shepard<sup>4</sup>, S. Shi<sup>115</sup>, Y. Shibata<sup>116</sup>, G. Shin<sup>62</sup>, D. Shiraki<sup>19</sup>, R. Shousha<sup>3</sup>, H. Si<sup>35</sup>, P. Simmerling<sup>117</sup>, G. Sinclair<sup>4</sup>, J. Sinha<sup>27</sup>, P. Sinha<sup>2</sup>, G. Sips<sup>4</sup>, T. Sizyuk<sup>29</sup>, C. Skinner<sup>2</sup>, A. Sladkomedova<sup>15</sup>, T. Slendebroek<sup>21</sup>, J. Slief<sup>20</sup>, R. Smirnov<sup>16</sup>, J. Smith<sup>4</sup>, S. Smith<sup>4</sup>, D. Smith<sup>26</sup>, J. Snipes<sup>27</sup>, G. Snoep<sup>118</sup>, A. Snyder<sup>4</sup>, P. Snyder<sup>4</sup>, E. Solano<sup>119</sup>, W. Solomon<sup>4</sup>, J. Song<sup>120</sup>, A. Sontag<sup>26</sup>, V. Soukhanovskii<sup>1</sup>, J. Spendlove<sup>121</sup>, D. Spong<sup>19</sup>, J. Squire<sup>4</sup>, C. Srinivasan<sup>55</sup>, W. Stacey<sup>48</sup>, G. Staebler<sup>4</sup>, L. Stagner<sup>21</sup>, T. Stange<sup>6</sup>, P. Stangeby<sup>50</sup>, R. Stefan<sup>4</sup>, R. Stempok<sup>4</sup>, D. Stephan<sup>4</sup>, J. Stillerman<sup>18</sup>, T. Stoltzfus-Dueck<sup>2</sup>, W. Stonecipher<sup>4</sup>, S. Storment<sup>15</sup>, E. Strait<sup>4</sup>, D. Su<sup>4</sup>, L. Sugiyama<sup>18</sup>, Y. Sun<sup>35</sup>, P. Sun<sup>35</sup>, Z. Sun<sup>2</sup>, A. Sun<sup>49</sup>, D. Sundstrom<sup>4</sup>, C. Sung<sup>122</sup>, J. Sungcoco<sup>4</sup>, W. Suttrop<sup>6</sup>, Y. Suzuki<sup>8</sup>, T. Suzuki<sup>5</sup>, A. Svyatkovskiy<sup>3</sup>, C. Sweet<sup>26</sup>, R. Sweeney<sup>18</sup>, C. Sweetnam<sup>2</sup>, G. Szepesi<sup>55</sup>, M. Takechi<sup>5</sup>, T. Tala<sup>113</sup>, K. Tanaka<sup>8</sup>, X. Tang<sup>91</sup>, S. Tang<sup>15</sup>, Y. Tao<sup>35</sup>, R. Tao<sup>4</sup>, D. Taussig<sup>4</sup>, T. Taylor<sup>4</sup>, K. Teixeira<sup>4</sup>, K. Teo<sup>63</sup>, A. Theodorsen<sup>123</sup>, D. Thomas<sup>4</sup>, K. Thome<sup>4</sup>, A. Thorman<sup>124</sup>, A. Thornton<sup>55</sup>, A. Ti<sup>35</sup>, M. Tillack<sup>16</sup>, N. Timchenko<sup>125</sup>, R. Tinguely<sup>18</sup>, R. Tompkins<sup>4</sup>, J. Tooker<sup>4</sup>, A. Torrezan De Sousa<sup>4</sup>, G. Trevisan<sup>0</sup>, S. Tripathi<sup>15</sup>, A. Trujillo Ochoa<sup>126</sup>, D. Truong<sup>65</sup>, C. Tsui<sup>16</sup>, F. Turco<sup>17</sup>, A. Turnbull<sup>4</sup>, M. Umansky<sup>1</sup>, E. Unterberg<sup>19</sup>, P. Vaezi<sup>16</sup>, P. Vail<sup>3</sup>, J. Valdez<sup>4</sup>, W. Valkis<sup>16</sup>, B. Van Compernelle<sup>4</sup>, J. Van Galen<sup>20</sup>, R. Van Kampen<sup>118</sup>, M. Van Zeeland<sup>4</sup>, G. Verdoolaege<sup>68</sup>, N. Vianello<sup>25</sup>, B. Victor<sup>1</sup>, E. Viezzer<sup>30</sup>, S. Vincena<sup>15</sup>, M. Wade<sup>19</sup>, F. Waelbroeck<sup>11</sup>, J. Wai<sup>3</sup>, T. Wakatsuki<sup>5</sup>, M. Walker<sup>4</sup>, G. Wallace<sup>18</sup>, R. Waltz<sup>4</sup>, W. Wampler<sup>65</sup>, L. Wang<sup>35</sup>, H. Wang<sup>35</sup>, Y. Wang<sup>35</sup>, H. Wang<sup>4</sup>, Z. Wang<sup>60</sup>, H. Wang<sup>60</sup>, Z. Wang<sup>2</sup>, Y. Wang<sup>37</sup>, G. Wang<sup>15</sup>, S. Ward<sup>87</sup>, M. Watkins<sup>4</sup>, J. Watkins<sup>65</sup>, W. Wehner<sup>4</sup>, Y. Wei<sup>17</sup>, M. Weiland<sup>6</sup>, D. Weisberg<sup>4</sup>, A. Welander<sup>4</sup>, A. White<sup>18</sup>, R. White<sup>2</sup>, S. Wiesen<sup>127</sup>, R. Wilcox<sup>19</sup>, T. Wilks<sup>18</sup>, M. Willensdorfer<sup>6</sup>, H. Wilson<sup>87</sup>, A. Wingen<sup>19</sup>, M. Wolde<sup>4</sup>, M. Wolff<sup>1</sup>, K. Woller<sup>18</sup>, A. Wolz<sup>110</sup>, H. Wong<sup>15</sup>, S. Woodruff<sup>42</sup>, M. Wu<sup>35</sup>, Y. Wu<sup>115</sup>, S. Wukitch<sup>18</sup>, G. Wurden<sup>91</sup>, W. Xiao<sup>128</sup>, R. Xie<sup>11</sup>, Z. Xing<sup>3</sup>, X. Xu<sup>1</sup>, C. Xu<sup>2</sup>, G. Xu<sup>115</sup>, Z. Yan<sup>26</sup>, X. Yang<sup>88</sup>, S. Yang<sup>2</sup>, T. Yokoyama<sup>129</sup>, R. Yoneda<sup>15</sup>, M. Yoshida<sup>5</sup>, K. You<sup>12</sup>, T. Younkin<sup>23</sup>, J. Yu<sup>4</sup>, M. Yu<sup>12</sup>, G. Yu<sup>37</sup>, Q. Yuan<sup>35</sup>, L. Zaidenberg<sup>130</sup>, L. Zakharov<sup>131</sup>, A. Zamengo<sup>4</sup>, S. Zamperini<sup>23</sup>, M. Zarnstorff<sup>3</sup>, E. Zeger<sup>15</sup>, K. Zeller<sup>4</sup>, L. Zeng<sup>15</sup>, M. Zerbini<sup>132</sup>, L. Zhang<sup>35</sup>, X. Zhang<sup>35</sup>, R. Zhang<sup>35</sup>, B. Zhang<sup>35</sup>, J. Zhang<sup>35</sup>, J. Zhang<sup>35</sup>, L. Zhao<sup>24</sup>, B. Zhao<sup>11</sup>, Y. Zheng<sup>37</sup>, L. Zheng<sup>11</sup>, B. Zhu<sup>1</sup>, J. Zhu<sup>18</sup>, Y. Zhu<sup>37</sup>, Y. Zhu<sup>38</sup>, M. Zsuttu<sup>4</sup>, M. Zuin<sup>25</sup>

Email: [fenstermacher1@llnl.gov](mailto:fenstermacher1@llnl.gov)

<sup>1</sup>Lawrence Livermore National Laboratory, <sup>2</sup>Princeton Plasma Physics Laboratory, <sup>3</sup>Princeton University, <sup>4</sup>General Atomics, <sup>5</sup>QST, <sup>6</sup>Max-Planck Institute for Plasma Physics, <sup>7</sup>Imperial College London, <sup>8</sup>National Institute for Fusion Science, Japan, <sup>9</sup>Mt. Holyoke College, <sup>10</sup>University of Sao Paulo, Institute of Physics, <sup>11</sup>University of Texas, Austin, <sup>12</sup>National Fusion Research Institute, <sup>13</sup>ITER-India, <sup>14</sup>College of William and Mary, <sup>15</sup>University of California, Los Angeles, <sup>16</sup>University of California, San Diego, <sup>17</sup>Columbia University, <sup>18</sup>Massachusetts Institute of Technology, <sup>19</sup>Oak Ridge National Lab, <sup>20</sup>Eindhoven University of Technology, <sup>21</sup>Oak Ridge Associated Universities, <sup>22</sup>West Virginia University, <sup>23</sup>University of Tennessee, Knoxville, <sup>24</sup>Far-Tech, Inc., <sup>25</sup>Consorzio RFX, <sup>26</sup>University of Wisconsin, <sup>27</sup>ITER Organization, <sup>28</sup>Stony Brook University (SUNY), <sup>29</sup>Purdue University, <sup>30</sup>University of Seville, <sup>31</sup>Universidad de Ingenieria y Tecnologia, <sup>32</sup>The College of William and Mary, <sup>33</sup>Carnegie Mellon University, <sup>34</sup>Institute for Plasma Research, India, <sup>35</sup>ASIPP, <sup>36</sup>Peking University, <sup>37</sup>University of California, Davis, <sup>38</sup>University

of California, Irvine, <sup>39</sup>Commonwealth Fusion Systems, <sup>40</sup>University of Liverpool, <sup>41</sup>EPFL, <sup>42</sup>Woodruff Scientific Incorporated, <sup>43</sup>Convergent Technologies, <sup>44</sup>Xantho Technologies, LLC, <sup>45</sup>University of Illinois, Urbana-Champaign, <sup>46</sup>Università di Milano-Bicocca, <sup>47</sup>CREATE Consortium, <sup>48</sup>Georgia Tech, <sup>49</sup>Southwestern Institute of Physics, China, <sup>50</sup>University of Toronto, <sup>51</sup>Auburn University, <sup>52</sup>Politecnico di Torino, <sup>53</sup>Instituto Superior Tecnico, Lisboa, Portugal, <sup>54</sup>Palomar College, <sup>55</sup>CCFE, <sup>56</sup>Kungliga Tekniska Hogskolan, <sup>57</sup>San Diego State University, <sup>58</sup>Istituto di Fisica del Plasma CNR-EURATOM, <sup>59</sup>Durham University, <sup>60</sup>Lehigh University, <sup>61</sup>Aalto University, <sup>62</sup>Korea National Fusion Research Center, <sup>63</sup>University of Washington, <sup>64</sup>CompX, <sup>65</sup>Sandia National Lab, <sup>66</sup>Tech-X Corporation, <sup>67</sup>Ulsan National Institute of Science and Technology, <sup>68</sup>Ghent University, <sup>69</sup>Technical University of Denmark, <sup>70</sup>CEA Cadarache, <sup>71</sup>Drake University, <sup>72</sup>Kalling Software, <sup>73</sup>University of Colorado, Boulder, <sup>74</sup>Harvard University, <sup>75</sup>National Technical University of Athens, <sup>76</sup>Coventry University, <sup>77</sup>EUROfusion, <sup>78</sup>SLS2 Consulting, <sup>79</sup>STI Optronics, Inc., <sup>80</sup>University of Stuttgart, <sup>81</sup>Baylor University - CASPER, <sup>82</sup>Institute of Plasma Physics AS CR, Czech Republic, <sup>83</sup>Alphawave Research, <sup>84</sup>Harvey Mudd College, <sup>85</sup>Seoul National University, <sup>86</sup>Donghua University, <sup>87</sup>University of York, <sup>88</sup>Dalian University of Technology, <sup>89</sup>University of California, Berkeley, <sup>90</sup>AKIMA Infrastructure Services, <sup>91</sup>Los Alamos National Laboratory, <sup>92</sup>Zap Energy Inc., <sup>93</sup>Department of Energy, <sup>94</sup>D-TACQ Solutions Ltd, <sup>95</sup>Inst. of Control Sciences of the Russian Academy of Sciences, <sup>96</sup>Fusion for Energy Joint Undertaking, <sup>97</sup>Palomar Scientific Instruments, Inc., <sup>98</sup>Astro Fusion Spectre LLC, <sup>99</sup>University of British Columbia, <sup>100</sup>Pacific Northwest National Laboratory, <sup>101</sup>ORISE, <sup>102</sup>Michigan State University, <sup>103</sup>Ishikawa National College of Technology, <sup>104</sup>Peak Technical Staffing, <sup>105</sup>University of Strathclyde, <sup>106</sup>Pennsylvania State University, <sup>107</sup>Rensselaer Polytechnic Institute, <sup>108</sup>University of Southern California, <sup>109</sup>Chalmers University of Technology (Sweden), <sup>110</sup>University of Virginia, <sup>111</sup>Università di Napoli Federico II, <sup>112</sup>Oxford University, <sup>113</sup>VTT Technical Research Centre, <sup>114</sup>Jefferson Lab, <sup>115</sup>University of Science and Technology of China, <sup>116</sup>National Institute of Technology, Gifu College, <sup>117</sup>University of Connecticut, <sup>118</sup>DIFFER, <sup>119</sup>Ciemat, <sup>120</sup>Hanyang University, <sup>121</sup>Brigham Young University, <sup>122</sup>KAIST, <sup>123</sup>UiT The Arctic University of Norway, <sup>124</sup>Australian National University, <sup>125</sup>RRC Kurchatov Institute, <sup>126</sup>Universidad Nacional de Ingeniería, <sup>127</sup>Forschungszentrum Juelich, <sup>128</sup>Zhejiang University, <sup>129</sup>University of Tokyo, <sup>130</sup>University of Michigan, <sup>131</sup>LiWFusion, <sup>132</sup>ENEA C.R. Frascati

## Abstract

DIII-D physics research addresses critical challenges for operation of ITER and the next generation of fusion energy devices. This is done through a focus on innovations to provide solutions for high performance long pulse operation, coupled with fundamental plasma physics understanding and model validation, to drive scenario development by integrating high performance core and boundary plasmas. Substantial increases in off-axis current drive efficiency from an innovative top launch system for EC power, and in pressure broadening for Alfvén eigenmode control from a co-/counter- $I_p$  steerable off-axis neutral beam, all improve the prospects for optimization of future long pulse/steady state high performance tokamak operation. Fundamental studies into the modes that drive the evolution of the pedestal pressure profile and electron vs. ion heat flux validate predictive models of pedestal recovery after ELMs. Understanding the physics mechanisms of ELM control and density pumpout by 3D magnetic perturbation fields leads to confident predictions for ITER and future devices. Validated modelling of high-Z shattered pellet injection for disruption mitigation, runaway electron dissipation, and techniques for disruption prediction and avoidance including machine learning, give confidence in handling disruptivity for future devices. For the non-nuclear phase of ITER, two actuators are identified to lower the L-H threshold power in hydrogen plasmas. With this physics understanding and suite of capabilities, a high poloidal beta optimized-core scenario with an internal transport barrier that projects nearly to  $Q=10$  in ITER at  $\sim 8$  MA was coupled to a detached divertor, and a near Super H-mode optimized-pedestal scenario with co- $I_p$  beam injection was coupled to a radiative divertor. The Hybrid core scenario was achieved directly, without the need for anomalous current diffusion, using off-axis current drive actuators. Also, a controller to assess proximity to stability limits and regulate  $\beta_N$  in the ITER baseline scenario, based on plasma response to probing 3D fields, was demonstrated. Finally, innovative tokamak operation using a negative triangularity shape showed many attractive features for future pilot plant operation.

## 1. INTRODUCTION

The mission of the DIII-D program is to provide a physics basis for the optimization of tokamak operations for fusion energy production. This is done through a continuous process of facility enhancements, experimental studies targeting fundamental physics understanding of mechanisms critical to future fusion power plant operation, and experiments to test candidate scenarios integrating optimized core and edge plasma performance. These advances are then used to validate key physics-based models and increase confidence in the use of those models for predictions of future device performance and optimization. Recent progress in each of these areas is described below.

This paper is organized as follows. Section 2 describes innovative facility and algorithm upgrades that have been used to address key aspects of core plasma performance optimization in reactor relevant regimes. Studies of selected solutions to physics issues critical to reactor operations are described in Section 3. These results are brought together in studies of integrated core-edge scenarios applicable to optimized power plant operation in Section 4. Conclusions and a future outlook are given in Section 5.

## 2. INNOVATIVE SOLUTIONS FOR HIGH PERFORMANCE LONG PULSE OPERATION

Experiments using recent hardware upgrades in DIII-D contribute to providing the physics basis for optimizing future steady state tokamak performance. In particular, upgrades to the neutral beam injection (NBI) and electron cyclotron heating (ECH) systems have allowed experiments to achieve greater control of the current and pressure profiles to improve performance and stability. The off-axis NBI power in DIII-D was increased by a factor of  $\sim 2$ , increasing both the off-axis pressure and current density for Advanced Tokamak (AT) scenarios. By launching from a higher poloidal angle with a nearly vertical beam trajectory in the poloidal plane projection, “top launch” off-axis EC current drive efficiency was doubled. Additional high-density off-axis wave heating and current drive can be provided by a High Harmonic Fast Wave (HHFW) helicon system. Detailed results will be given below.

The new and unique co-/counter- $I_p$  steerable off-axis neutral beam [1] recently installed in DIII-D improves performance of steady state tokamak scenarios by reducing losses of energetic beam ions due to various instabilities [2]. Successful creation of a high- $q_{min}$  steady state scenario in the ITER Fusion Power Operation (FPO) phase, and in future advanced tokamak reactors, depends on the ability to optimize the current profile. While reverse shear increases thermal confinement, the co-alignment of the location of  $q_{min}$  and the steep fast-ion pressure gradient drives Reversed Shear Alfvén Eigenmodes (RSAEs), which have been shown previously to cause fast ion transport that degrades core performance in DIII-D [2]. The new experiments have shown that injection of beam power away from the magnetic axis drives off-axis current [1] in agreement with NUBEAM predictions, and it also broadens the energetic particle (EP) pressure profile [3]. Fig. 1a shows that both the thermal pressure increases and beam pressure gradient decreases using the new increased off-axis neutral beam power. The combination of  $q_{min}$  moving to slightly smaller radius and the central fast ion pressure profile broadening, both due to the off-axis NBI, reduces the fast ion pressure gradient in the region of  $q_{min}$ . This reduces RSAE drive and increases both core thermal pressure and the maximum achieved ratio of the measured neutron rate to the predicted neutron rate, assuming classical fast ion slowing down (Fig. 1a) in scenarios at high toroidal rotation. Fast-ion confinement, indicated by the ratio of measured vs. predicted neutrons without AE instability losses, improved by 25% during flat-top using the new off-axis NBI (Fig. 1b). In the current ramp, further improvements to optimize the  $q$ -profile using Electron Cyclotron Current Drive (ECCD) resulted in  $\sim 36\%$  higher measured neutron ratio than the reference shot. Record parameters of  $\beta_N \sim 3.1$  and  $H_{89} \sim 2.2$  were achieved for this scenario near the upper end of the DIII-D field capability ( $B_T = 2.0$  T) and  $q_{95} = 6.0$ . These experiments demonstrate an effective fast-ion loss minimization principle that can be used to guide optimization of high- $q_{min}$  operation in ITER and future reactors.

The achievement of more than double the off-axis ECCD efficiency using top launch geometry, compared with conventional low field side (LFS) launch [4, 5], provides a path to substantially increase the off-axis current critical to optimization of the performance and minimization of the cost of future steady state fusion reactors. A prototype top launch system with fixed toroidal and poloidal injection angles utilizing second harmonic X-mode damping was installed on DIII-D to experimentally validate and characterize this approach. Here “top launch” geometry refers to injection from near the top of the device on the high field side of the magnetic axis, and with a nearly vertical beam trajectory in the poloidal plane projection (Fig. 2a). As predicted by CQL3D quasi-linear Fokker-Planck simulations, and verified by experiments which vary the wave-electron interactions in the velocity space by scanning  $B_T$  (Fig. 2b), the significant enhancement of the ECCD efficiency in the top launch experiments compared with outside launch (Fig. 2c) was due to interaction with higher  $v_{||}$  electrons that suffer fewer collisions and drive current more efficiently, combined with a longer absorption path for the EC waves to compensate for inherently weaker absorption at higher  $v_{||}$ . For higher  $v_{||}$  interaction (lower  $B_T$ ) the absorbed EC power was observed to decrease, giving rise to a “sweet spot” (optimal  $B_T$ ) for maximum ECCD efficiency (Fig. 2b), where the higher current drive efficiency for higher  $v_{||}$  is balanced by sufficient absorption. Orienting this sweet spot for absorption vs current drive efficiency at mid-radius, the driven current was 2x higher than for outside launch (Fig. 2c). This complete understanding of the mechanisms for enhanced ECCD from top launch geometry can be used to optimize future ECCD systems for power plant scenario needs.



The effectiveness of fast emergency shutdown for disruption prevention during plasma current rampdown after locked mode detection in single-null plasmas at ITER-relevant normalized-currents shows that with optimization at least 50% of rampdown disruptions were delayed until after the plasma current  $I_p$  was reduced to ITER-safe normalized-current levels (Fig. 3a) [6]. Key to the shutdown result is for the  $I_p$  ramp down phase to transition to an inner wall limited (IWL) shape after the locked mode precursor to disruption is detected and emergency rampdown initiated. The overall disruptivity during  $I_p$  rampdown was also reduced for IWL rampdowns compared with diverted rampdowns. The applicability of this technique to ITER is under consideration, but the effectiveness achieved points to the importance of early prevention techniques and reliable mitigation tools.

A recently developed algorithm for real-time regulation of proximity-to-instability boundaries has been applied for robust Vertical Displacement Event (VDE) prevention in DIII-D experiments [6]. The algorithm uses either a physics-based or neural-net-based VDE growth-rate estimation to monitor stability, and modifies plasma shaping in real-time to prevent the growth-rate from reaching uncontrollable limits. Figs. 3b and 3c show that the controller engages only when it detects that the VDE growth rate has exceeded a pre-programmed threshold value. The VDE is then prevented by real time reduction of the plasma elongation and separatrix to inner wall gap to prevent further increases in the VDE growth rate. Once again, the key for the control is to detect the approach to vertical instability and to modify the plasma shape to maintain stability control. Finally, a novel technique for healing locked mode flux surfaces with 3D fields demonstrated promise for providing current quench control by allowing the plasma to partially reheat and thereby extend the Current Quench (CQ) to a long timescale [7]. In this technique the stochastic field line state at the start of the thermal quench is healed by the applied 3D fields into a 3D helical equilibrium with intact flux surfaces, allowing the plasma temperature to partially recover and substantially extending the quench time to final loss of current. This suggests a possible method for a soft-landing of plasma disruptions in the high plasma current regime. Taken together these results show substantial progress toward development of the algorithms and control actuators needed for both disruption/VDE avoidance and mitigation in ITER and future devices.

Studies of high current runaway electron (RE) beams [8,9] reveal excitation of current-driven (low edge safety factor,  $q_a$ )  $m/n=2/1$  kink instabilities (Fig. 4) that promptly terminate the RE beam on an Alfvénic time-scale, with minimal heating of plasma facing component surfaces [10,11], offering a new alternate pathway to RE beam mitigation without collisional dissipation. MARS-F modelling [9] predicts that the absence of wall heating is due to both an increase of the wetted area during the MHD-driven RE loss (Fig. 4e,f) and an inhibition of the conversion of magnetic energy into kinetic energy normally observed during RE loss events (when the RE beam regenerates during CQ). Observations of IR emission from the centerpost during RE beam loss (Fig. 4f) confirm the MARS-F predictions that the wetted area would include the full toroidal and a substantial poloidal range after the MHD event disperses the RE beam. The experiment also confirms that no RE beam regeneration occurs and instead the original RE current transfers to the cold bulk, which then dissipates the magnetic energy on the timescale of a cold resistive plasma. Variations of  $D_2$  purity by comparisons with experiments using high-Z impurity injection revealed that high  $D_2$  purity was required to obtain recombination of the bulk plasma. This decreased the density and shortened the Alfvén time facilitating access to the required low  $q_a$  regime and accelerating the large-scale MHD instability terminating the RE beam and preventing the RE regeneration. This result is highly applicable to ITER and future reactors in which the initial RE beam will quickly avalanche to high current and drive edge safety factor low enough to promote the  $2/1$  kink instability needed to disperse the RE beam. Initial simulations for ITER scenarios in pure deuterium plasma [10] suggest a multi-step process of RE regeneration, hydrogenic plasma purification and kink mode RE beam dispersal may be required to fully dissipate all remaining RE current, due to the extremely high RE amplification factors anticipated in ITER.

Particle assimilation rates and Current Quench (CQ) densities for single and multiple Shattered Pellet Injection (SPI) containing high-Z material (e.g. Neon) are shown to be predictable from 0-D global energy balance simulations and also from empirical scaling laws, without invoking anomalous MHD mode mixing physics [12]. Straightforward predictions of neon SPI assimilation have been successful by assuming the CQ plasma is radiation limited. The simulations use the 0D KPRAD model [13,14] with an SPI ablation model that tracks species dependent shielding-limited ablation [15] of the SPI plume, main-ion and impurity ionization, recombination and radiation, Ohmic heating and inductive coupling to wall currents. The modelled CQ density evolution agreed well with measurements for neon SPI in DIII-D ohmic, standard H-mode and Super H-mode plasmas (Fig. 5a-c). Also, in an H-mode plasma similar to that in Fig. 5b before the SPI, the simulated CQ density evolution with two SPI pellets injected within 200ms of each other was very similar to the measurements (Fig. 5d). For deuterium SPI, global energy balance

modelling does not match the CQ density evolution and data show that MHD mixing plays a significant role in the CQ timescales [16]. Data and simulations also show toroidal radiation peaking during the thermal quench with single high-Z SPI is close to but not exceeding the factor of 2 surface melt limit [17] set for ITER. Empirical scaling laws for the average current quench density during neon SPI assimilation derived from global parameters like plasma stored energy, and average electron density and temperature are also consistent with global energy balance being the dominant physics. These experiments show that the optimization of global behavior for multiple, high-Z, Shattered Pellet Injection should now be predictable for ITER and future reactors

### 3. FUNDAMENTAL PLASMA PHYSICS UNDERSTANDING AND MODEL VALIDATION THAT ADVANCE FUSION SOLUTIONS

Plasma rotation scans, and both new non-linear analytic theory [18,19] and non-linear 2-fluid code simulations [20,21], confirm that ELM suppression by 3D Magnetic Perturbations (3DMPs) requires near zero ExB velocity at the top of the pedestal, and achieving suppression appears to be closely linked to a high field side plasma response. Predictions from substantive recent advances in non-linear theory of 3DMP penetration in rotating plasmas [18,19] are consistent with non-linear simulations of resonant field penetration using the TM1 [22] and GPEC [23] codes, and results from DIII-D experiments. Using experimental parameters and RMP amplitudes (Fig. 6a), TM1 correctly predicts the RMP amplitude required for a bifurcation from screening to penetration of resonant fields at the pedestal top, and also calculates the reduction in the pedestal height and width due to collisional transport across these islands (Fig. 6b). The observed density pump-out is reproduced (Fig. 6b) from the MHD simulations for the penetration of resonant fields in the resistive foot of the pedestal [20]. From these simulations ELM suppression is seen to correlate with approximately a 15% decrease in the pedestal electron pressure ( $p_{e^{ped}}$ ) compared with EPED predictions (Figs. 6a,b). The TM1 simulations also quantitatively explain the required plasma density, rotation and RMP amplitude for the ELM suppression by  $n = 2$  RMPs due to the formation of magnetic islands at the top of the pedestal [21]. These MHD simulations reveal strong screening of resonant fields in the steep gradient region between the top and the foot of the pedestal, consistent with the preservation of the edge electron thermal barrier (ETB) during pump-out and ELM suppression.

The long-standing mystery of the  $q_{95}$  width of ELM suppression windows has been effectively resolved based on simulations of resonant field penetration at the pedestal top [24,25]. The TM1 simulations successfully predict that narrow magnetic islands form when resonant field penetration occurs at the top of pedestal, and these islands are easily screened when  $q_{95}$  moves off resonance, leading to very narrow windows of ELM suppression (typically  $\Delta q_{95} \sim 0.1$  as shown in Figs. 6a,b). For the radial perturbation field used in the experiment (Fig. 6c horizontal dashed line), the prediction for the  $q_{95}$  ELM suppression windows comes from the windows having at least 15%  $p_{e^{ped}}$  degradation as calculated by TM1 (Fig. 6b). TM1 accurately predicts the separated  $q_{95}$  windows in which ELM suppression is seen in experiments (width and  $q_{95}$  ranges of yellow bands in Figs. 6a,b vs regions with greater than 15%  $p_{e^{ped}}$  reduction at the experimental radial field in Fig. 6c) with  $n=3$  structure 3DMPs. TM1 also predicts the observed amount of density pumpout by 3DMPs (Fig. 6b). A database of TM1 simulations over a broad operating space in pedestal density and ExB rotation has been compared with DIII-D ELM suppression results [21] to generate a dimensional scaling relation for the 3DMP penetration threshold. The scaling agrees well with results of full TM1 simulations of ITER cases using predicted baseline kinetic and ExB profiles. The predicted ELM suppression windows (regions with at least 15%  $p_{e^{ped}}$  reduction) for  $n=3$  and  $n=4$  structure 3DMPs (Figs. 6d and 6e) suggest [25] that ELM suppression should be possible in the ITER  $q_{95} \sim 3.1$  range using significantly less than the 90kAt 3DMP coils currents available in the ITER design. In addition, the  $n=4$  results in particular show that at the 90kAt limit there may be substantial overlap of  $q_{95}$  windows, thereby retaining ELM suppression for a range of plasma currents from about 11-15 MA in ITER [25]. Finally, ELM suppression with 3DMPs is not observed in double-null diverted configurations [26] consistent with theory and code predictions that a high field side response is required for 3DMP field penetration in order to limit pedestal growth that drives the ELM instability. These advances provide the ability to accurately optimize the use of the 3DMP coil set in ITER and future devices for ELM suppression over a wide range of plasma operating parameters, including techniques for minimizing the density pumpout [27] and L-H power threshold increases [28,29] associated with 3DMP ELM control, and for achieving ELM suppression during variations in plasma current and edge safety factor.

Advances in pedestal physics through new measurements of density and internal magnetic fluctuations, and advances in non-linear simulations, suggest that variations of the electron and ion heat fluxes are consistent with the

evolution of multi-scale turbulence in the pedestal. These studies [30-36] identify possible roles for Ion Temperature Gradient (ITG), Micro-Tearing and Trapped Electron Modes (MTMs and TEMs) in DIII-D pedestal transport. In DIII-D experiments with pedestal ion collisionality  $\nu_i^* = 0.9$ , observations immediately after the ELM crash show that ITG scale density fluctuations (Fig. 7a), predominantly at the bottom of the pedestal, drive ion and electron thermal transport [30]. The density gradient and  $E_r$  well reform rapidly and ITG is suppressed by ExB shear, consistent with the decrease of pedestal ion heat flux ( $Q_i$ ) from anomalous to near neoclassical. Main ion CER measurements indicate pedestal  $Q_i$  becomes increasing anomalous at low collisionality, but at high collisionality  $Q_i$  in the pedestal region remains closer to neoclassical [31,32]. On the longer timescale of the electron temperature gradient recovery, the TEM turbulence (Fig. 7b) exhibits a threshold in electron temperature gradient (Fig. 7c) and then saturates later in the ELM recovery. MTM scale electro-magnetic modes (Fig 7d) driven by  $\text{grad-}T_e$  can also contribute to the anomalous  $Q_e$  through to the end of the ELM cycle as suggested by non-linear simulations [32-34], although their experimental identification is not yet conclusive in this set of experiments. Finally, simulations predict that Electron Temperature Gradient (ETG) modes also contribute to  $Q_e$  between ELMs [36], although the spatial scales are so short that no direct measurements of ETG scale fluctuations in the pedestal are available. This detailed understanding of the turbulent thermal transport drives in the pedestal significantly improves our ability to understand inter-ELM pedestal transport for projections to ITER and future devices.

To contribute to the ITER Research Plan urgent tasks, recent experiments with hydrogen plasmas in DIII-D at low input torque, similar to the first ITER non-nuclear Pre Fusion Power Operation (PFPO-1) phase, show that the L-H power threshold was reduced [28,29,37] with either small admixtures of helium or by using non-resonant 3DMP fields to produce edge counter-current Neoclassical Toroidal Viscosity (NTV) torque (Fig. 8). Low rotation H-mode operation of hydrogen plasma was achieved in these experiments with a combination of toroidally balanced hydrogen NBI and ECH power.  $P_{L-H}$  was reduced about 30% (Fig. 8a) by adding  $\leq 20\%$  helium ions to the hydrogen plasma for densities spanning the broad minimum in  $P_{L-H}$ . The  $P_{L-H}$  threshold in hydrogen plasma without helium seeding was also reduced 20-30% (Fig 8b) at ITER relevant input torque using  $n=3$  non-resonant 3D perturbation fields from the DIII-D external coils at 3DMP levels consistent with the capabilities of the ITER internal coils. These experiments identify two actuators that could be used to reduce the L-H power threshold in the non-nuclear phase of ITER, where H-mode access is likely challenging in particular at high fractions of the Greenwald density.

The ability to predict the impurity seeding needed for divertor dissipation has advanced through the new capability for measuring charge-state resolved densities of impurity species in the divertor [38] and validation of SOL and divertor fluid modelling with full poloidal and radial drifts. By combining EUV/VUV measurements of resonance emission lines [39] with local electron density and temperature measurements from Thomson scattering and a collisional radiative model framework, the 2D density distributions of all the charge states of carbon (examples in Fig. 9a) were calculated for the DIII-D divertor plasma in both attached and detached H-mode conditions. UEDGE simulated profiles (Figs. 9b and 9c) were quantitatively much closer to the measured 2D distributions when full poloidal and radial drifts were included in the modelling (Fig. 9b) than for corresponding simulations without the drifts (Figs. 9c). Note that for the example plasma shown, the experimental data indicates the outer divertor is detached, which is consistent with the fractional abundances of  $C1^+$ ,  $C2^+$  and  $C3^+$  all being peaked progressively farther off the target plate poloidally as charge state increases. The simulation with drifts reproduces these characteristics of the charge state distributions in detachment, but the case without drifts shows a qualitatively incorrect fully attached outer leg with these charge states peaking very near the target surface. This qualitative difference in the simulations emphasizes the importance of including the full radial and poloidal drifts in the calculations. The data showed that fractional abundance of the various charge states within the total carbon density had a strong spatial variation, as did the total carbon density normalized to the electron density. These fractional abundances were also strong functions of the divertor conditions; the measured carbon fraction of the electron density decreased by 10x from attached to detached conditions, with similar but slightly smaller reduction factors in the comparison of simulations with full drift effects. The carbon fraction needed for strike point detachment estimated from simplified 1D SOL models (e.g., [40-42]) was about a factor of 2 higher than inferred from these detailed 2D data. These data will validate and improve aspects of the fluid code modelling with full drifts, and the validated codes are directly applicable to ITER relevant scenarios in which other impurity species (e.g., nitrogen or neon) are proposed to be used for divertor detachment control.

With these advances, experimental data using impurity injection and SOLPS-ITER simulations with full drift effects show that for the Small Angle Slot (SAS) baffling geometry in the upper divertor of DIII-D, divertor detachment and pedestal performance can be optimized through magnetic geometry and choice of impurity species [43,44]. Experiments with nitrogen injection show that a larger quantity of impurity is required to detach the SAS divertor plasma (Fig. 10a), and a higher density of nitrogen appears in the pedestal and core plasma (Fig. 10b) when the Outer Strike Point (OSP) is in the outer corner of the slot (red) compared with the OSP positioned on the inner slanted surface of the SAS (blue) [43,44]. SOLPS-ITER modelling with full cross-field drifts and both carbon and nitrogen impurity charge states is required to reproduce these effects. The modeling shows that the differences are due to changes in the stagnation point location of the main ion cross field flow profiles and changes in the entrainment of nitrogen ions in those flows as a result of the geometry change [44]. Experiments using the optimum magnetic geometry with the OSP on the inner slanted baffle in the SAS found that the choice of impurity species (Neon vs Nitrogen) injected into the SAS outer leg had little effect on the upstream pedestal Te profiles (Fig. 10d), but the pedestal density gradient was significantly higher and separatrix density significantly lower with Neon injection (Fig. 10c). These experiments, and the comparison to modelling with full drifts and impurity charge states, increases confidence in predictions of divertor detachment optimization by choice of strike point geometry and impurity species

Simulations of the radial migration of tungsten from a nearly toroidally continuous ring embedded in the carbon divertor tiles (Fig. 11b) reproduce the observed redeposition of a W:C layer outboard of the source ring only when ExB drift effects are taken into account (Fig. 11a) [45,46]. These simulations and measurements were taken from the DIII-D campaign of Lower Single Null (LSN) plasmas with the tungsten ring in the lower divertor [47]. Mixed material DIVIMP-WallDYN modelling [45] including ExB drifts is more consistent with the observed redeposition profile (diamonds in Fig. 11a) than modelling that neglects ExB drifts; however, simulations using 60% of the theoretical drifts for the attached L-mode conditions of the experiment turn out to be more consistent with measurements than predictions assuming the full theoretical magnitude of the drifts. This result suggests that additional physics such as the effect of SOL currents on the calculated radial electric field need to be taken into account in the magnitude of the ExB drifts. This work identifies the important physics controlling the radial migration both in terms of the mixed material environment relevant to the W, Be situation in ITER and the importance of the poloidal particle drifts, which will be very strong in many phases of ITER operation.

Modelling of intra-ELM tungsten gross erosion from the continuous toroidal ring [47] with an analytic Free-Streaming plus Recycling Model (FSRM) [48,49] is now validated in ITER-relevant mitigated-ELM regimes using pellet pacing and RMPs (Figs. 11c and 11d) [48]. For pellet paced ELMs the FSRM reproduces the observation that the peak intra-ELM W gross erosion is reduced compared with natural ELMs (Fig. 11c). In this case the pedestal  $n_e$  and  $T_e$  remained nearly constant but the ELM frequency was increased 2x by the pellets and, as a consequence, the pedestal carbon content was decreased almost a factor of 2. Since intra-ELM W sputtering is strongly affected by C6+ ions, the reduction in pedestal carbon content contributed to the reduction in W erosion, as reproduced by the FSRM. For ELM size mitigated but not completely suppressed by 3D magnetic fields (Fig. 11d), the FSRM again reproduces the observation that the peak intra-ELM W gross erosion increases slightly compared with natural ELMs. In this case the effect of the 3D fields was to reduce the upstream pedestal density at nearly constant pedestal temperature, and thereby produce a strong reduction in the divertor target density and a 20% increase in target  $T_e$ . By taking the effects of these changes in target plasma conditions properly into account, the FSRM again reproduced the intra-ELM W sputtering evolution. These experiments, with a radially localized source of tungsten, help to validate erosion and redeposition models to increase predictability of tungsten behavior in ITER.

#### 4. SCENARIOS INTEGRATING HIGH PERFORMANCE CORE AND BOUNDARY

Integration of a high-performance core plasma and a low temperature solution for the plasma at the divertor targets has been demonstrated in a high poloidal beta scenario that features large Shafranov shift, Internal Transport Barriers (ITBs) in  $n_e$ ,  $T_e$  and  $T_i$  coupled to a detached divertor using active feedback-controlled  $N_2$  or Ne puffing [50-54]. Theory-based modelling suggests that similar plasmas in ITER Fusion Power Operation (FPO) phase with planned heating systems could be consistent with  $Q=10$  at reduced plasma current of 7-9MA [51]. In the DIII-D experiments, feedback control of either nitrogen or neon was used to control the degree of detachment of the divertor while coupling to a high-performance core plasma at high poloidal beta (nitrogen case shown in Fig. 12) [50, 52, 53]. This example shows the characteristics of the core-edge coupling achieved with either nitrogen or neon

impurity seeding. With sufficient impurity injection (Fig. 12b) the ion saturation current at the divertor outer strike point achieves roll over and the electron temperature measured with probes drops below 5eV across the entire divertor plate (Fig. 12c). At the same time pedestal pressure is also reduced due to impurity radiation but high central core pressure is retained (Fig. 12a). Injection of the impurity in the divertor helped to trigger the formation of an internal transport barrier at large radius in the core density, and both electron and ion temperature profiles, compensating for the reduction in pedestal pressure and enhancing the performance parameters to  $H_{98y2} = 1.5$ ,  $\beta_N = 3$ ,  $\beta_p > 2$ , at  $q_{95} = 7.8$ . In separate high  $\beta_p$  experiments, large radius ITBs were also obtained with strong deuterium gas injection [52,53]. The high  $\beta_p$  configuration lends itself to ITB formation due to a combination of Shafranov shift stabilization of turbulence, high bootstrap current generation at high  $q_{95}$  and high  $q_{min}$  at large radius [54]. Impurity injection and radiation at the plasma edge enhances the redistribution of bootstrap current from near the very edge to a large radius ( $\rho=0.7-0.8$ ) location in the core as the pedestal pressure and its gradient are reduced (Fig. 12d). This current redistribution decreases the local magnetic shear at this location allowing the plasma to self-organize to a stable low transport state with high local pressure gradients (the ITB). The experiments with Neon injection also demonstrated suppression of ELMs during the coupling of high core performance and a detached divertor [52]. Based on these results, self-consistent equilibrium and 1D transport modelling of an ITER scenario, using the TGLF code with the same turbulence saturation rule that matches the measured profiles in simulations of the DIII-D discharges, shows that the  $Q=10$  goal for ITER is predicted at  $I_p=7-9$  MA,  $\beta_N=2.8$  and  $P_{fus} = 300$  MW using the ITER day-one heating systems [51]. This represents a possible alternate scenario to achieve the  $Q=10$  ITER mission at lower risk to the device from disruptions and Type-I ELMs due to the reduced plasma current. The high  $\beta_p$  scenario at this reduced current is also predicted to achieve ITER's 500 MW fusion power goal at  $Q\sim 40$ , albeit with higher  $\beta_N\sim 3.2$ . The DIII-D experiments validate the simulation predictions of ITB formation and high performance in an ITER high  $\beta_p$  scenario at reduced plasma current.

High density and stored energy plasmas with Super H-mode (SH) edge pedestals [55, 56] were made both in a lower single null (LSN) shape accessible by JET [57] and in a higher triangularity near double null shape coupled at least transiently to a radiative divertor [58] for target heat flux control using nitrogen injection for substantial ( $\sim 80\%$ ) radiated power fraction in a core-edge integrated scenario (Fig. 13). Super H-mode pedestal operation has also been obtained in an upper single null (USN) shape with a more closed divertor baffling configuration. Prior to the LSN experiment, calculations with EPED [59] predicted that enhanced pedestal pressure in the SH channel would be accessible in a LSN plasma with moderate shaping accessible in JET. Stationary operating points at peeling-limited pedestal pressures far up the SH channel were achieved (Fig. 13a), although at lower absolute pressures than obtained transiently for SH operation in highly shaped double null (DN) plasmas [58]. The pedestal pressure in these high-density plasmas was about 40% higher than comparable plasmas in the same LSN shape operating with a ballooning limited pedestal at similar densities (Fig. 13a). Building on these results, EPED analysis of ITER LSN scenarios showed potential for operation in the SH-mode channel with up to a 50% enhancement of the pedestal pressure compared with H-mode [57, 60].

In the SH-mode experiments with highly shaped DN plasmas [58], simultaneous pedestal operation for several energy confinement times at the entrance to the SH-mode channel and radiative divertor operation with divertor strike points at the onset of detachment was obtained using nitrogen injection (Fig. 13b,c,d). In these cases the pedestal pressure remained on the second stability solution at the entrance to the SH channel (Fig. 13b), and higher than for standard H-mode in the same shape, for several energy confinement times after impurity injection [57, 58]. Total radiated power fraction in these discharges was up to 80% of the input power dominantly in the lower divertor and exceeding the 70% radiated power fraction target for ITER scenarios. Divertor line radiation (Fig. 13c,d) confirmed that  $T_e$  near the outer strike point was reduced to  $\sim 4$ eV (Fig. 13d) and  $T_e$  in the SOL near the X-point was reduced to  $\sim 10$ eV (Fig. 13c). In addition, target  $T_e$  and ion saturation current ( $J_{sat}$ ) from floor probes, and the observed 30% reduction of the measured outer divertor strike point (OSP) heat flux, confirmed the OSP was at the onset of detachment during the time the high pedestal pressure was maintained [58]. Advanced control algorithms [61,62] were used to achieve these results including the use of feedback-controlled 3D fields for density control and feedback nitrogen gas puffing for divertor radiated power control. All of these results suggest that it may be desirable to look into SH-like pedestal pressure enhancements in ITER scenarios with detached radiative divertors.

TRANSP simulations confirm that a high-performance hybrid core scenario, experimentally maintained with  $q_0 > 1$  (Fig. 14) and no sawteeth using off-axis ECCD, could be explained directly from the calculated off-axis driven current without invoking anomalous current diffusion physics [63]. In previous TRANSP simulations of hybrid core

operation with on-axis ECCD (Fig. 14a), the simulated evolution of central safety factor,  $q_0$ , without invoking anomalous current diffusion physics did not match the measurement. Simulations of the experiments with off-axis ECCD matched the evolution of  $q_0$  well using only the calculated profiles of the driven current (Fig. 14b). Similar performance of the steady state hybrid regime with on-axis ECCD was also achieved using off-axis ECCD aimed at  $\rho=0.45$  (Fig. 14c), with no sawteeth for greater than 1.5 current diffusion times,  $\beta_N=3.7$ ,  $H_{98y2}=1.6$  and  $q_{95}=6$ . These high beta, high density hybrid scenarios in DIII-D project with  $\rho^*$  scaling to  $Q=5$  in ITER at  $I_p=8.3$  MA and pedestal Greenwald fraction of 0.9. Also high-performance hybrids were demonstrated to be compatible with radiative divertor operation using Neon or Argon gas injection [64]. Core impurity peaking in these hybrids was substantially reduced using near-axis ECH heating. This new demonstration of control of current profile broadening in hybrid core plasmas increases confidence in steady state  $Q > 5$  ITER hybrid scenarios with off-axis current drive

Experiments in the ITER baseline scenario showed that the plasma magnetic response to oscillating probing fields provided a sensor for assessing proximity to stability limits and regulating  $\beta_N$  [65]. MARS-F simulations of resistive MHD, with plasma rotation included, reproduced the dependence of the plasma response to sinusoidal probing fields of various frequencies with variation of rotation,  $\bar{i}$  and  $\beta_N$ . Using Active Magnetic Spectroscopy (AMS) frequency and amplitude scans, a controller was optimized and demonstrated that the plasma response could be kept away from levels correlated with mode locking by feedback on the injected NB power [65]. This suggests that AMS could be an attractive technique, applicable to ITER and future devices, for avoiding stability limits.

Finally, plasma scenarios with an innovative negative triangularity shape were obtained with high confinement factor, significant normalized beta and an L-mode like edge without ELMs [66-69]. A database of timeslices for both inner wall limited and LSN diverted negative triangularity plasmas (Fig. 15a) shows confinement factors  $H_{98y2}$  up to 1.4 and  $\beta_N$  up to 3.0. Detailed TRANSP analysis of the highest performing of these plasmas is underway, with indications the confinement enhancement may be slightly lower ( $H_{98y2}$  up to 1.2). High power injection into a LSN diverted shape with large average negative triangularity maintained an L-mode edge without ELMs up to 5x the L-H power threshold scaling for positive triangularity. Stability analysis for the edge of these plasmas showed that ballooning modes closed off the access to second stability and prevented growth of the pedestal to the ELM instability boundary [69]. The scaling of the total stored energy with injected power in these plasmas was significantly stronger than that predicted by the ITER-89P scaling law, which was derived for positive or near-zero triangularity. Plasmas with marginally less negative average triangularity developed an H-mode edge and ELMs at the normal L-H threshold power, suggesting a threshold in the degree of negative triangularity needed to retain the L-mode edge [68]. The SOL width in the L-mode edge cases without ELMs was up to 50% broader than the inter-ELM SOL width for the H-mode case at slightly less negative triangularity (Fig. 15b). Normalized impurity particle confinement in the strongly negative triangularity diverted shapes was low ( $\tau_{imp}/\tau_E \sim 1$ ) consistent with the L-mode edge, no central impurity accumulation and  $Z_{eff} \sim 1.5$ . These initial observations are all attractive features of the negative triangularity plasma shape for projections toward future fusion pilot plants.

## 5. SUMMARY AND FUTURE PLANS

The DIII-D physics program is addressing critical challenges for operation of ITER and the next generation of fusion energy devices through a focus on innovative solutions for high performance steady state operation, coupled with fundamental plasma physics understanding and model validation, which drives the development of scenarios that integrate high performance core and boundary plasmas. Recent experiments have combined new injected power systems and increased understanding of physics mechanisms, to optimize several candidate core-edge integrated scenarios for future fusion pilot plants.

Progress has been made toward the goals of validated heating and current drive models applicable to ITER and current profile control techniques for optimization of future steady state tokamak reactors [70]. Use of an additional off-axis neutral beam injector from a recently upgraded 5MW co-/counter- $I_p$  steerable beamline reduced the fast ion losses due to AE instabilities and improved the performance of Advanced Tokamak (AT) high  $q_{min}$  scenarios. Vertical top launch of EC power increased the ECCD efficiency by a factor of 2 for off-axis deposition. Calculations indicate that planned High Harmonic Fast Wave (HHFW) injection [70-73] with a recently installed helicon antenna, and planned unique High Field Side (HFS) Lower Hybrid (LH) slow wave injection [70, 74] will contribute substantially to the ability to control the current profile in the high-density core plasmas [75] needed to couple to effective radiative divertor solutions in DIII-D.

Significant progress has been made to address critical issues for ITER operation including in the areas of disruption prediction, avoidance and mitigation, runaway electron beam dissipation, ELM control, H-mode operation in the non-nuclear phase, and material migration from target erosion. New machine learning based proximity-to-instability algorithms connected to plasma shape actuators were effective to avoid VDEs. After detection of pending disruption, inner-wall-limited techniques for emergency plasma shutdown were effective to ramp down  $I_p$  below the required ITER limits before any disruption. Experiments find that at high RE current density (low rational edge safety factor) and in the presence of deuterium injection, a large external kink instability terminates the entire high energy runaway population and disperses it over a large area of the wall, while also avoiding RE regeneration. Non-linear simulations can now predict the isolated  $q_{95}$  windows where ELM suppression is expected to occur from the application of 3D magnetic perturbation fields. Two different techniques within ITER's capabilities were shown to significantly lower the L-H power threshold for dominantly hydrogen plasmas characteristic of the planned ITER non-nuclear phases. Direct measurement of impurity charge state distributions for both attached and detached divertor operation now challenge and validate 2D SOL and divertor plasma models, identifying the critical role of poloidal and radial cross field drifts. Results from impurity injection into the SAS divertor also challenge and validate the SOL and divertor fluid codes with full drift effects. Finally experiments showed that explaining observed tungsten migration required taking into account effects due to ExB drifts, and tungsten erosion during ELMs mitigated by several techniques had a strong dependence on the effect of the technique on the plasma conditions near the target surface.

Recent developments in integrating high performance core and edge solutions showed promise in plasmas with high poloidal beta and an internal transport barrier, plasmas with an enhanced Super H-mode pedestal pressure, plasmas with a Hybrid core having central  $q_0 > 1$ , and plasmas with a high negative triangularity shape. Plasmas with a high  $\beta_p$  and an ITB facilitated by divertor impurity injection (Nitrogen or Neon) showed excellent core performance parameters simultaneously with detached low heat and particle flux divertor target plasma. Highly shaped plasmas with elevated Super H-mode pedestal pressure were coupled to a radiative divertor at the onset of strike point detachment using nitrogen injection. Experiments also demonstrated access to enhance SH-mode pedestal pressure in moderately shaped LSN plasmas accessible in JET and ITER. Plasmas with increased off-axis current drive sustained hybrid core operation at high  $\beta_N$  without sawteeth for multiple current diffusion times, and simulations showed that central  $q_0$  remained above 1.0 without invoking anomalous current diffusion physics. Finally, innovative plasmas with a strongly negative triangularity shape operated at good H-mode like confinement and core  $\beta_N$  but with an L-mode like edge, broad SOL heat flux width and no ELMs. Each of these scenarios displays many of the features needed to optimize tokamak operation in reactor relevant regimes.

In 2021 and beyond the DIII-D program will install additional tools for optimizing tokamak operation through core plasma current and heating profile control, and will continue work to couple high performance core operation to edge plasma solutions for steady state and transient heat and particle fluxes [70]. Core optimization through current and pressure profile control will be investigated using a 1 MW LFS helicon High Harmonic Fast Wave CD system [76], a unique HFS Lower Hybrid CD system [77], and increased ECH power including additional top launch injectors. Edge plasma and plasma materials interactions solutions will be explored using a new high power closed divertor geometry [78] and a wall insertion test station for macroscopic scale innovative materials testing. For the longer term, major upgrades to both the normalized and absolute capabilities of the facility are being considered to increase performance and flexibility in order to resolve the physics and techniques for integrated core-edge solutions in the relevant physics regimes for future fusion reactors. Additional issues critical to optimization of power plant performance would be addressed for example with proposed installation of a new high toroidal mode number array of internal midplane 3DMP coils [79] and a passive RE mitigation coil [80]. These and many other tools will enhance the ability of the DIII-D facility to address the important issues needed to provide the physics basis for optimizing the tokamak approach to fusion energy production.

## ACKNOWLEDGEMENTS

This material is based upon work supported by the U.S. Department of Energy, Office of Science, Office of Fusion Energy Sciences, using the DIII-D National Fusion Facility, a DOE Office of Science user facility, under Awards DE-FC02-04ER54698 and DE-AC52-07NA27344.



## DISCLAIMER

This report was prepared as an account of work sponsored by an agency of the United States Government. Neither the United States Government nor any agency thereof, nor any of their employees, makes any warranty, express or implied, or assumes any legal liability or responsibility for the accuracy, completeness, or usefulness of any information, apparatus, product, or process disclosed, or represents that its use would not infringe privately owned rights. Reference herein to any specific commercial product, process, or service by trade name, trademark, manufacturer, or otherwise does not necessarily constitute or imply its endorsement, recommendation, or favoring by the United States Government or any agency thereof. The views and opinions of authors expressed herein do not necessarily state or reflect those of the United States Government or any agency thereof.

## REFERENCES

- [1] GRIERSON, B., “Testing The DIII-D Co/Counter Off-Axis Neutral Beam Injected Power and Ability to Balance Injected Torque”, 28th IAEA Fusion Energy Conference (Proc. Int. Conf. Nice, France, 2021), IAEA, Vienna (2021), submitted to Nucl. Fus (2021).
- [2] COLLINS, C., “Improving Fast-Ion Confinement and Performance by Reducing Alfvén Eigenmodes in the  $q_{min}>2$ , Steady-State Scenario”, Preprint 28th IAEA Fusion Energy Conference (Proc. Int. Conf. Nice, France, 2021), IAEA, Vienna (2021) [EX/8-2]
- [3] PARK, J-M, “Off-axis Neutral Beam Current Drive for Advanced Tokamak”, Preprint 28th IAEA Fusion Energy Conference (Proc. Int. Conf. Nice, France, 2021), IAEA, Vienna (2021) [EX/P1-1/CN-286/1009]
- [4] CHEN, Xi, “Doubling Off-axis Electron Cyclotron Current Drive Efficiency Using Reactor-relevant ‘Top Launch’ in the DIII-D Tokamak”, PRL submitted (2021)
- [5] CHEN, Xi, “Doubling the Efficiency of Off-axis Current Drive Using Reactor-relevant ‘Top Launch ECCD’ on the DIII-D Tokamak”, Preprint 28th IAEA Fusion Energy Conference (Proc. Int. Conf. Nice, France, 2021), IAEA, Vienna (2021) [EX/1-TH/1 H & CD & Steady-state & Operation-1]
- [6] BARR, J.A., “Development and experimental qualification of novel disruption prevention techniques on DIII-D”, 28th IAEA Fusion Energy Conference (Proc. Int. Conf. Nice, France, 2021), IAEA, Vienna (2021), submitted to Nucl. Fus (2021).
- [7] DU, X., “Experimental Evidence of Runaway Electron Tail Generation via Localized Helical Structure in Pellet-triggered Tokamak Disruptions”, NF submitted (2021)
- [8] PAZ-SOLDAN, C., et al., “Kink Instabilities of the Post-Disruption Runaway Electron Beam at Low Safety Factor”, PPCF, 64, 054001 (2019).
- [9] PAZ-SOLDAN, C. “A novel path to runaway electron mitigation via current-driven kink instability”, 28th IAEA Fusion Energy Conference (Proc. Int. Conf. Nice, France, 2021), IAEA, Vienna (2021), submitted to Nucl. Fus (2021).
- [10] REUX, C. et al PRL accepted 2021
- [11] REUX, C. et al., “Magnetohydrodynamic simulations of runaway electron beam termination in JET”, PPCF, 63, 035024 (2021)
- [12] SHIRAKI, D. et al., “DIII-D and International Research Extrapolating Shattered Pellet Performance to ITER”, Preprint: 28th IAEA Fusion Energy Conference (Proc. Int. Conf. Nice, France, 2021), IAEA, Vienna (2021) [EX/5-TH/6 Disruption-2]
- [13] WHYTE, D. et al., “Disruption Mitigation with High-pressure Noble Gas Injection”, J. Nucl. Mater., 313-316, 1239 (2003)
- [14] HOLLMANN, E. et al., “0-D Modeling of Fast Radiative Shutdown of Tokamak Discharges Following Massive Gas Injection”, Contrib. Plasma Phys, 48, 260 (2008)
- [15] PARKS, P. et al., “A Theoretical Model for the Penetration of a Shattered-Pellet Debris Plume”, Theory and Simulation of Disruptions Workshop (2017), PPPL, Princeton NJ
- [16] SHIRAKI, D. et al., “Measurement and Modelling of Shattered Pellet Assimilation in DIII-D”, Bull. Am. Phys Soc. (2019).
- [17] SUGIHARA, M. et al., “Disruption scenarios, Their Mitigation and Operation Window in ITER” Nucl Fusion, 47, 337 (2007)
- [18] FITZPATRICK, R., Theory of edge localized mode suppression by static resonant magnetic perturbations in the DIII-D tokamak”, Phys Plasmas, 27, 042506 (2020)
- [19] FITZPATRICK, R., “An improved theory of the response of DIII-D H-mode discharges to static resonant magnetic perturbations and its implications for the suppression of edge localized modes”, Phys. Plasmas 27, 072501 (2020)
- [20] HU Q. M., et al., “The density dependence of edge-localized-mode suppression and pump-out by resonant magnetic perturbations in the DIII-D tokamak”, Phys. Plasmas 26, 120702 (2019).
- [21] HU Q. M., et al., “The role of edge resonant magnetic perturbations in edge-localized-mode suppression and density pump-out in low-collisionality DIII-D plasmas”, Nucl. Fusion 60, 076001 (2020).
- [22] YU Q. and Günter S., “Plasma response to externally applied resonant magnetic perturbations”, Nucl. Fusion 51, 073030 (2011).
- [23] PARK J.K. and LOGAN N.C., “Self-consistent perturbed equilibrium with neoclassical toroidal torque in tokamaks”, Phys. Plasmas 24, 032505 (2017).

- [24] HU Q.M., et al., “Wide Operational Windows of Edge-Localized Mode Suppression by Resonant Magnetic Perturbations in the DIII-D Tokamak”, *Phys. Rev. Lett.* 125 045001 (2020).
- [25] HU, Q.M., “Nonlinear two-fluid modeling of plasma response to RMPs for the ELM control in the ITER baseline”, 28th IAEA Fusion Energy Conference (Proc. Int. Conf. Nice, France, 2021), IAEA, Vienna (2021), submitted to *Nucl. Fus* (2021).
- [26] SHAFER, M. et al., “Limits of RMP ELM Suppression in Double Null”, Preprint: 28th IAEA Fusion Energy Conference (Proc. Int. Conf. Nice, France, 2021), IAEA, Vienna (2021) [EX/P1-1/CN-286/930]
- [27] LOGAN, N.C., “Improved Particle Confinement with 3D Magnetic Perturbations in DIII-D H-mode Plasmas”, *Bull. Am. Phys. Soc.*, (2021), to be submitted to *Nuclear Fusion*.
- [28] SCHMITZ, L., “L–H transition trigger physics in ITER-similar plasmas with applied  $n = 3$  magnetic perturbations”, *Nucl. Fusion* 59 126010 (2019)
- [29] KRIETE, M., “Effect of magnetic perturbations on turbulence-flow dynamics at the L-H transition on DIII-D”, *Physics of Plasmas* 27, 062507 (2020)
- [30] BARADA, K., “New understanding of multi-scale/multi-field pedestal turbulence, transport, and gradient behavior during type-I ELMs on the DIII-D tokamak”, 28th IAEA Fusion Energy Conference (Proc. Int. Conf. Nice, France, 2021), IAEA, Vienna (2021), submitted to *Nucl. Fus* (2021).
- [31] HASKEY, S., “Main-ion thermal transport in high performance DIII-D edge transport barriers”, Preprint: 28th IAEA Fusion Energy Conference (Proc. Int. Conf. Nice, France, 2021), IAEA, Vienna (2021) [EX/P1-1/CN-286/750]
- [32] NELSON, A.O., “Dynamical Evolution of Plasma Microinstabilities in Tokamaks”, *Nucl. Fusion* submitted (2021)
- [33] HATCH, D.R. “Microtearing modes as the source of magnetic fluctuations in the JET pedestal”, *Nucl. Fusion* 61 036015, (2021)
- [34] HASSAN, E. “Identifying the Microtearing Modes in the pedestal of DIII-D H-modes using Gyrokinetic Simulations”, submitted to *Nuclear Fusion* (2021).
- [35] CHEN, J., “Pedestal Magnetic Turbulence Measurements in ELMy H-Mode Plasmas In DIII-D Tokamak”, Preprint: 28th IAEA Fusion Energy Conference (Proc. Int. Conf. Nice, France, 2021), IAEA, Vienna (2021) [EX/P1-1/CN-286/682]
- [36] GUTTENFELDER, W. “Testing predictions of electron scale turbulent pedestal transport in two DIII-D ELMy H-modes “, *Nucl. Fusion* 61 056005 (2021), <https://doi.org/10.1088/1741-4326/abcc7>.
- [37] L. SCHMITZ, et al., “Reducing the L-H Transition Power Threshold via Neoclassical Toroidal Viscosity, Edge Rotation Reversals, and Shape Changes”, Preprint: 28th IAEA Fusion Energy Conference (Proc. Int. Conf. Nice, France, 2021), IAEA, Vienna (2021) [EX/P1-1/CN-286/1007]
- [38] SAMUELL, C (MCLEAN, A.G.), “Advancements in Understanding the 2D Role of Impurity Radiation for Dissipative Divertor Operation on DIII-D”, 28th IAEA Fusion Energy Conference (Proc. Int. Conf. Nice, France, 2021), IAEA, Vienna (2021) [EX/P1-1/CN-286/867]
- [39] MCLEAN, A.G, “Extreme and Vacuum Ultraviolet Spectroscopy in the Divertor of DIII-D”, *Rev. Sci. Instrum.*, (2020).
- [40] GOLDSTON, R.J., “Heuristic drift-based model of the power scrape-off width in low-gas-puff H-mode tokamaks”. *Nucl. Fusion* 52, 013009 (2012).
- [41] GOLDSTON, R.J., “Theoretical aspects and practical implications of the heuristic drift SOL model”, *J. Nucl. Mater.*, 463, 397-400 (2015).
- [42] GOLDSTON, R.J. “Generalization of the Heuristic Drift SOL Model for Finite Collisionality, and Effect on Flow Shearing Rate vs. Interchange Growth Rate”, *Bull. Am. Phys. Soc.*, (2020), *Phys Plasmas* submitted (2021)
- [43] CASALI, L. “Improved core-edge compatibility using impurity seeding in the small angle slot (SAS) divertor at DIII-D”, *Phys. Plasmas*, 27, 062506 (2020)
- [44] CASALI, L. et al., “Improved impurity retention and pedestal performance in DIII-D closed divertor”, 28th IAEA Fusion Energy Conference (Proc. Int. Conf. Nice, France, 2021), IAEA, Vienna (2021)
- [45] NICHOLS, J., “Modeling of ExB effects on tungsten re-deposition and transport in the DIII-D divertor,” *NF* accepted (2021), <https://iopscience.iop.org/article/10.1088/1741-4326/ac14e6>, <https://doi.org/10.1088/1741-4326/ac14e6>.
- [46] ABRAMS, T. et al., “Advances in Understanding High-Z Sourcing, Migration, and Transport on DIII-D from L-mode to High-Performance Regimes”, Preprint: 28th IAEA Fusion Energy Conference (Proc. Int. Conf. Nice, France, 2021), IAEA, Vienna (2021) [EX/P1-1/CN-286/660]
- [47] UNTERBERG E.A. et al., “Localized divertor leakage measurements using isotopic tungsten sources during edge-localized mode-y H-mode discharges on DIII-D”, *Nucl. Fusion* 60, 1, (2020) 016028
- [48] ABRAMS, T. et al., “Experimental validation of a model for particle recycling and tungsten erosion during ELMs in the DIII-D divertor”, *Nucl. Mater. Energy* 17 (2018) 164–173
- [49] ABRAMS, T. et al., “Impact of ELM control techniques on tungsten sputtering in the DIII-D divertor and extrapolations to ITER”, *Phys. Plasmas* 26 (2019) 062504
- [50] WANG, L., “Achievements of Actively Controlled Divertor Detachment Compatible with Sustained High Confinement Core In DIII-D and EAST”, 28th IAEA Fusion Energy Conference (Proc. Int. Conf. Nice, France, 2021), IAEA, Vienna (2021), submitted to *Nucl. Fus* (2021).
- [51] DING, S., “A Low Plasma Current ( $\sim 8$  MA) Approach for ITER’s  $Q=10$  Goal”, 28th IAEA Fusion Energy Conference (Proc. Int. Conf. Nice, France, 2021), IAEA, Vienna (2021), submitted to *Nucl. Fus* (2021).
- [52] WANG, L., “Integration of full divertor detachment with improved core confinement for tokamak fusion plasmas”, *Nature Comm.* 12, 1365 (2021).

- [53] WANG, H.Q. *et al.*, “Observation of Fully Detached Divertor Integrated with Improved Core Confinement for Tokamak Fusion Plasmas”, *Phys. Plasmas* 28, 052507 (2021).
- [54] DING, S. JIAN, X., GAROFALO, A.M., “The Dominant Micro-Turbulence Instabilities in the Lower  $q_{95}$  High  $\beta_p$  Plasmas on DIII-D and Predict First Extrapolation”, *Nucl Fusion*, 60, 016023 (2020).
- [55] SNYDER, P.B. *et al.*, “Super H-mode: Theoretical prediction and initial observations of a new high-performance regime for tokamak operation”, *Nucl. Fusion* 55, 083026 (2015).
- [56] SNYDER, P. B. *et al.*, “High Fusion Performance in Super H-Mode Experiments on Alcator C-Mod And DIII-D”, *Nuc. Fusion*, 59, 086017 (2019).
- [57] KNOLKER, M, SNYDER, P.B., EVANS, T.E. *et al.*, “Optimizing the Super H-Mode Pedestal to Improve Performance and Facilitate Divertor Integration”, *Plas Phys* 27, 102506 (2020).
- [58] WILKS, T. “Development of an integrated core-edge scenario using the Super H-mode compatible with JET and ITER operation”, 28th IAEA Fusion Energy Conference (Proc. Int. Conf. Nice, France, 2021), IAEA, Vienna (2021), submitted to *Nucl. Fus* (2021).
- [59] SNYDER, P.B. “A first-principles predictive model of the pedestal height and width: development, testing and ITER optimization with the EPED model”, *Nucl. Fusion* 51 103016 (2011)
- [60] KNOLKER, M. “On the stability and stationarity of the Super H-mode combined with an ion transport barrier in the core”, *PPCF* 63 (2021) 025017
- [61] ELDON, D. *et al.*, “An Analysis of Controlled Detachment by Seeding Various Impurity Species in High Performance Scenarios on DIII-D and EAST”, *Nuclear Materials and Energy* 27, 100963 (2021)
- [62] LAGGNER, F. *et al.*, “Real-time pedestal optimization and ELM control with 3D fields and gas flows on DIII-D”, *Nucl. Fusion* 60 076004 (2020)
- [63] PETTY, C.C., “New Regime for High-Beta Hybrid Using Off-Axis Current Drive on DIII-D”, Preprint: 28th IAEA Fusion Energy Conference (Proc. Int. Conf. Nice, France, 2021), IAEA, Vienna (2021).
- [64] PETRIE, T.W. *et al.*, “High-performance double-null plasmas under radiating mantle scenarios on DIII-D”, *Nucl. Mat. And Energy*, 19, 267 (2019). [EX/P1-1/CN-286/950]
- [65] HANSON, J, “Resistive contributions to the stability of DIII-D ITER baseline demonstration discharges”, *Phys Plasmas*, Dec 2020
- [66] AUSTIN, M., “Achievement of reactor-relevant high normalized beta and high confinement with L mode edge in negative triangularity shape in DIII-D”, *PRL* 122, 115001, 2019.
- [67] MARINONI, A., “H-mode grade confinement in L-mode edge plasmas at negative triangularity on DIII-D”, *Phys. Plasmas* 26, 042515 (2019)
- [68] MARINONI, A., “Diverted Negative Triangularity Plasmas On DIII-D: The Benefit of High Confinement Without the Liability of An Edge Pedestal”, 28th IAEA Fusion Energy Conference (Proc. Int. Conf. Nice, France, 2021), IAEA, Vienna (2021), submitted to *Nucl. Fus* (2021).
- [69] SAARELMA, S. “Ballooning instability preventing the H-mode access in plasmas with negative triangularity shape on the DIII-D tokamak”, *Plasma Phys and Control Fusion*, (2021)
- [70] BUTTERY, R.J., “DIII-D Research to Prepare for Steady State Advanced Tokamak Power Plants”, *Journal of Fusion Energy* [https://doi.org/10.1007/s10894-018-0185-y\(0123456789\(\).,-volV\)\(0123456789\(\).,-volV\)](https://doi.org/10.1007/s10894-018-0185-y(0123456789().,-volV)(0123456789().,-volV))
- [71] PRATER, R. *et al.*, “Application of very high harmonic fast waves for off-axis current drive in the DIII-D and FNSF-AT tokamaks”, *Nucl. Fusion* 54 083024 (2014)
- [72] LAU, C. *et al.*, “AORSA full wave calculations of helicon waves in DIII-D and ITER”, *Nucl. Fusion* 58 066004 (2018)
- [73] PINSKER, R. I., “Whistlers, helicons, and lower hybrid waves: The physics of radio frequency wave propagation and absorption for current drive via Landau damping”, *Physics of Plasmas* 22, 090901 (2015); doi: 10.1063/1.4930135
- [74] WUKITCH, S.J., SHIRAIWA, S., WALLACE, G.M., BONOLI, P.T., HOLCOMB, C. and PINSKER, R.I., "High Field Side Lower Hybrid Current Drive Simulations for Off- axis Current Drive in DIII-D", 22<sup>nd</sup> Topical Conference on Radio-Frequency Power in Plasmas EPJ Web of Conferences 157, 02012 (2017), DOI: <https://doi.org/10.1051/epjconf/201715702012>.
- [75] GAROFALO, A. M., *et al.*, "Access to sustained high-beta with internal transport barrier and negative central magnetic shear in DIII-D", *Phys. Plasmas* 13, 056110 (2006)
- [76] VAN COMPERNOLLE, B., “The High-Power Helicon Program At DIII-D: Gearing Up for First Experiments”, 28th IAEA Fusion Energy Conference (Proc. Int. Conf. Nice, France, 2021), IAEA, Vienna (2021), submitted to *Nucl. Fus* (2021).
- [77] WUKITCH, S, “DIII-D High Field Side Lower Hybrid Current Drive: Experiment Overview”, 46th European Physical Society Conference on Plasma Physics, 2019
- [78] WANG, H-Q. *et al.*, “The Effect of Synergy Between Divertor Geometry and Drifts on Divertor Power Dissipation in the DIII-D Small Angle Slot Divertor”, Preprint: 28th IAEA Fusion Energy Conference (Proc. Int. Conf. Nice, France, 2021), IAEA, Vienna (2021) [EX/P2-2/CN-286/1499]
- [79] WEISBERG, D. “Optimizing multi-modal, non-axisymmetric plasma response metrics with additional coil rows on DIII-D”, *Nucl. Fusion* 59 086060 (2019)
- [80] WEISBERG, D. “Passive deconfinement of runaway electrons using an in-vessel helical coil”, *Nucl. Fusion* submitted (2021)

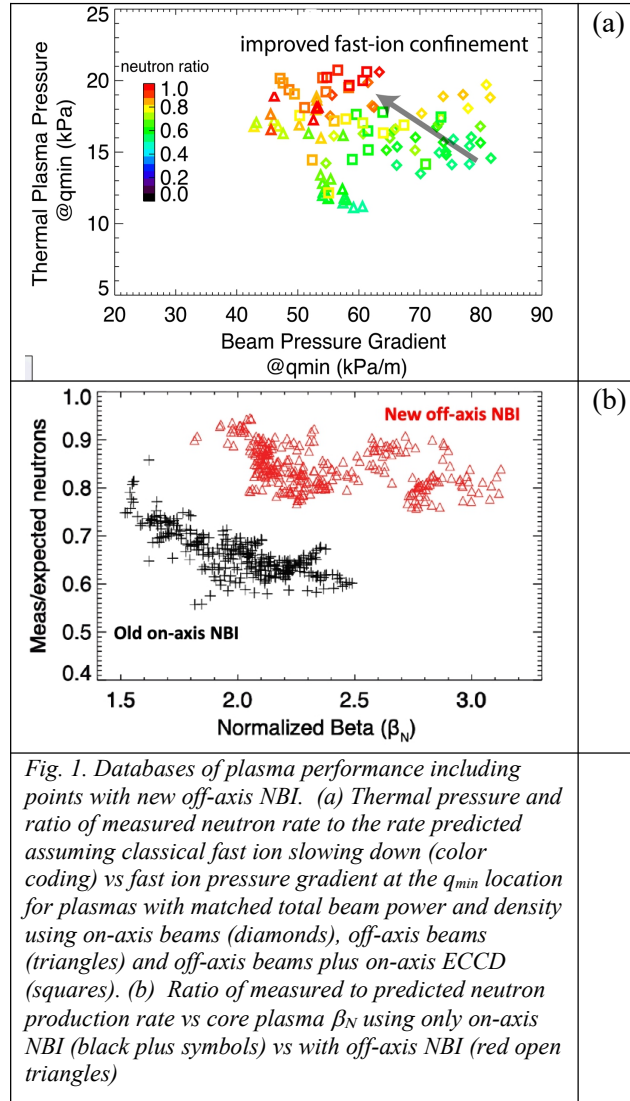
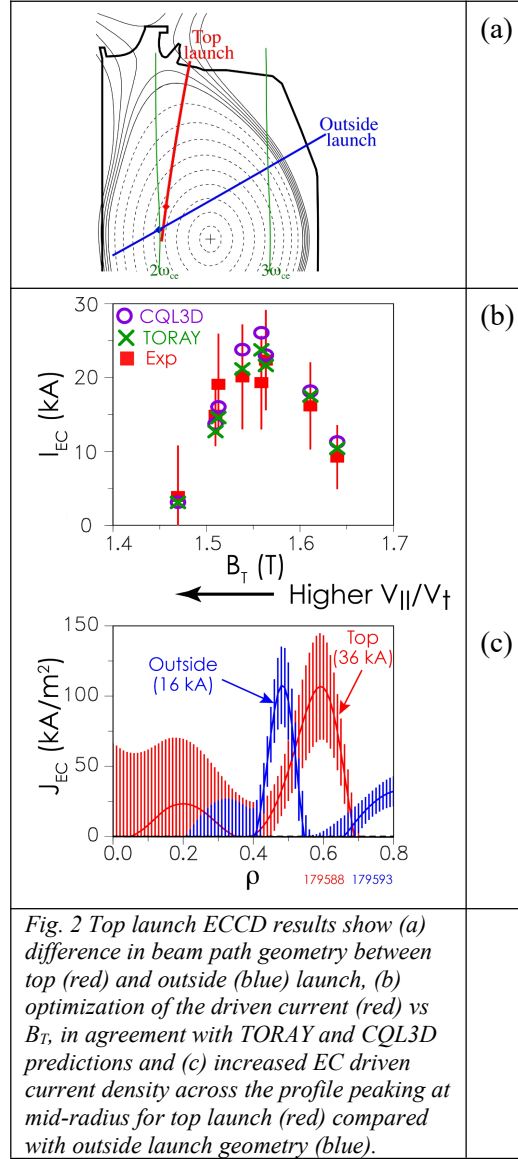
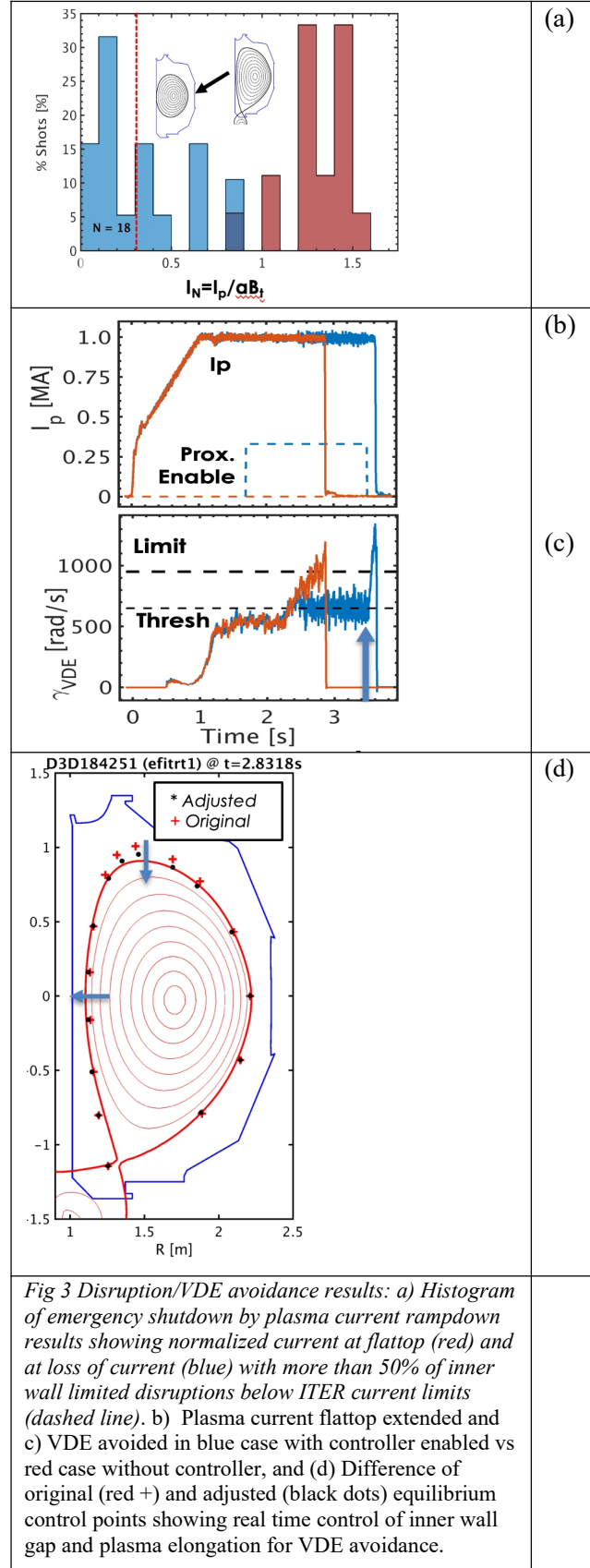


Fig. 1. Databases of plasma performance including points with new off-axis NBI. (a) Thermal pressure and ratio of measured neutron rate to the rate predicted assuming classical fast ion slowing down (color coding) vs fast ion pressure gradient at the  $q_{min}$  location for plasmas with matched total beam power and density using on-axis beams (diamonds), off-axis beams (triangles) and off-axis beams plus on-axis ECCD (squares). (b) Ratio of measured to predicted neutron production rate vs core plasma  $\beta_N$  using only on-axis NBI (black plus symbols) vs with off-axis NBI (red open triangles)





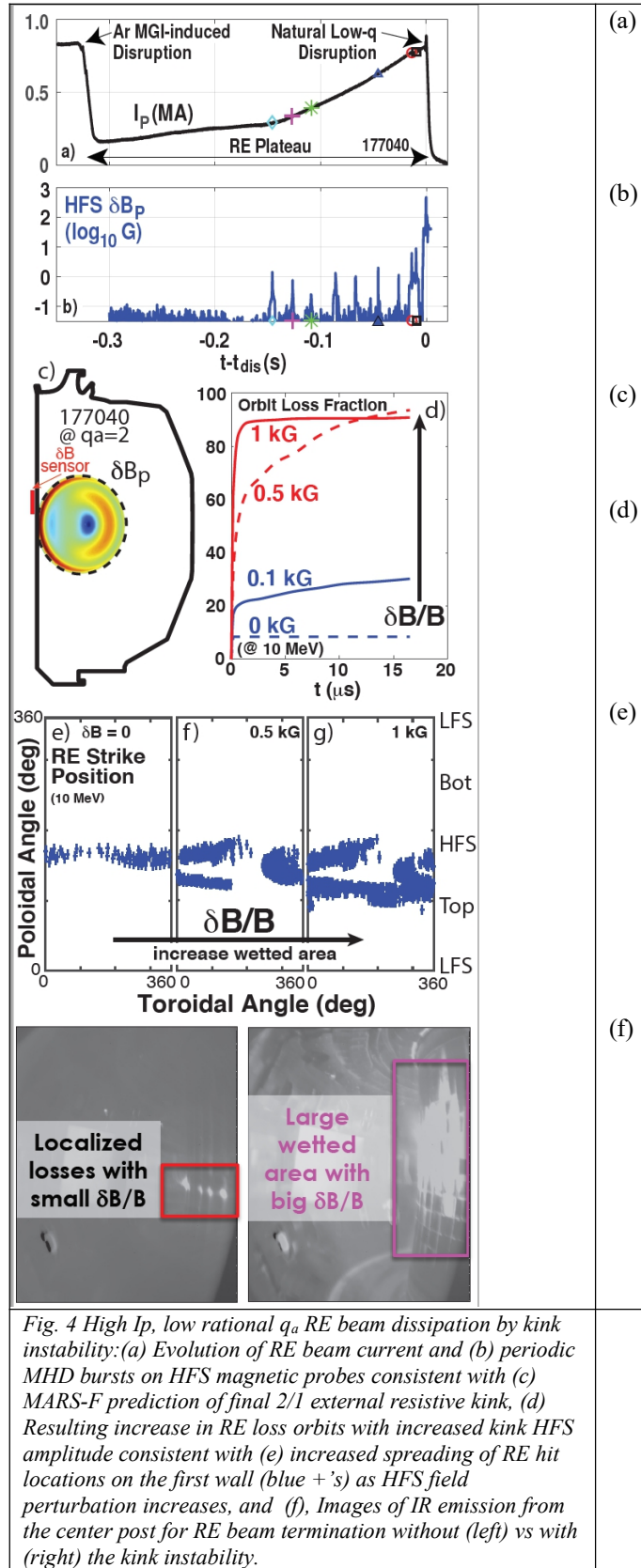
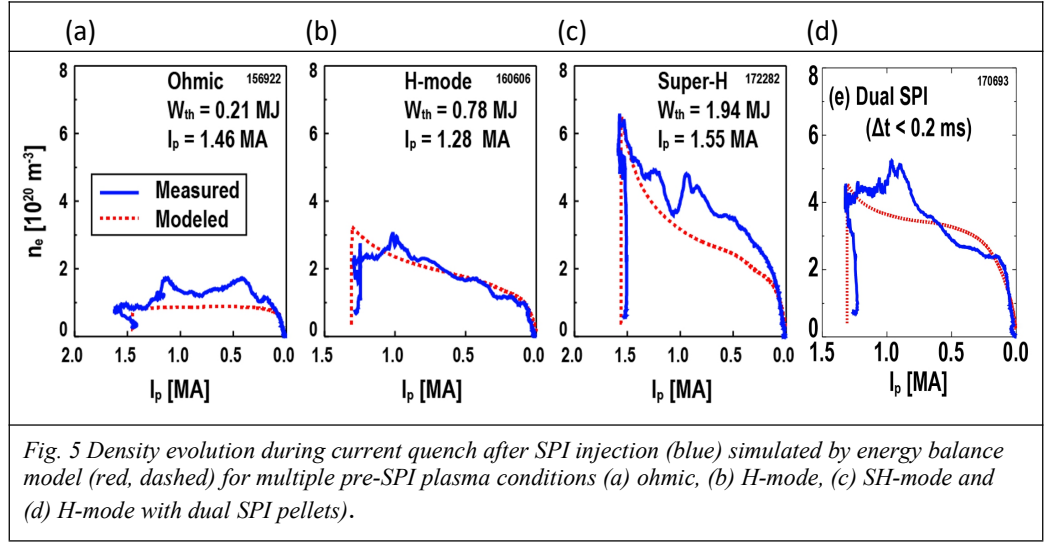


Fig. 4 High  $I_p$ , low rational  $q_a$  RE beam dissipation by kink instability: (a) Evolution of RE beam current and (b) periodic MHD bursts on HFS magnetic probes consistent with (c) MARS-F prediction of final 2/1 external resistive kink, (d) Resulting increase in RE loss orbits with increased kink HFS amplitude consistent with (e) increased spreading of RE hit locations on the first wall (blue + 's) as HFS field perturbation increases, and (f), Images of IR emission from the center post for RE beam termination without (left) vs with (right) the kink instability.





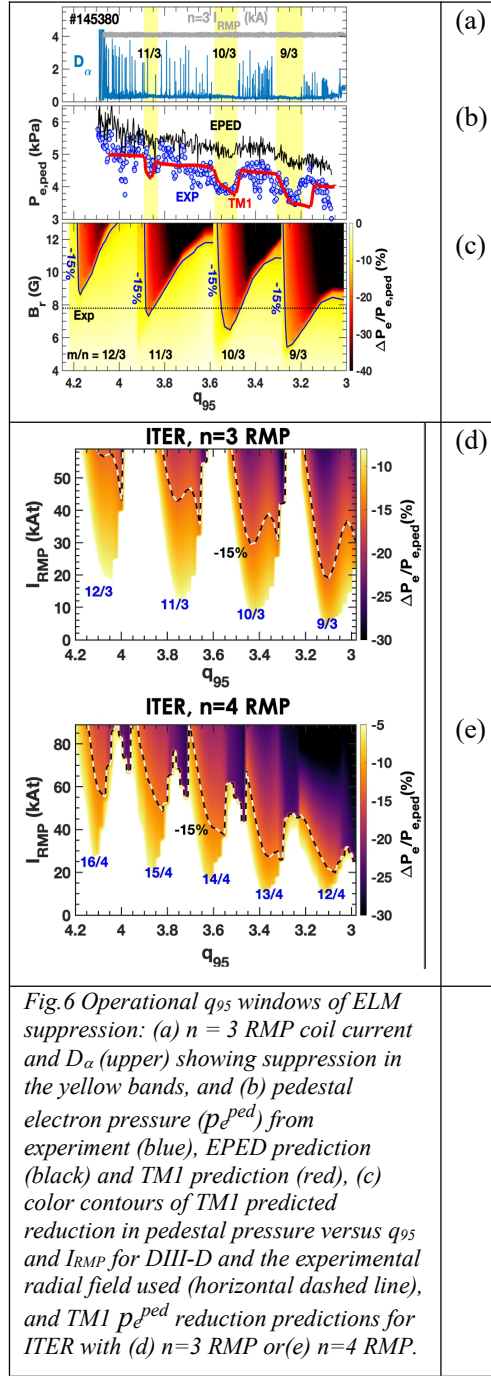
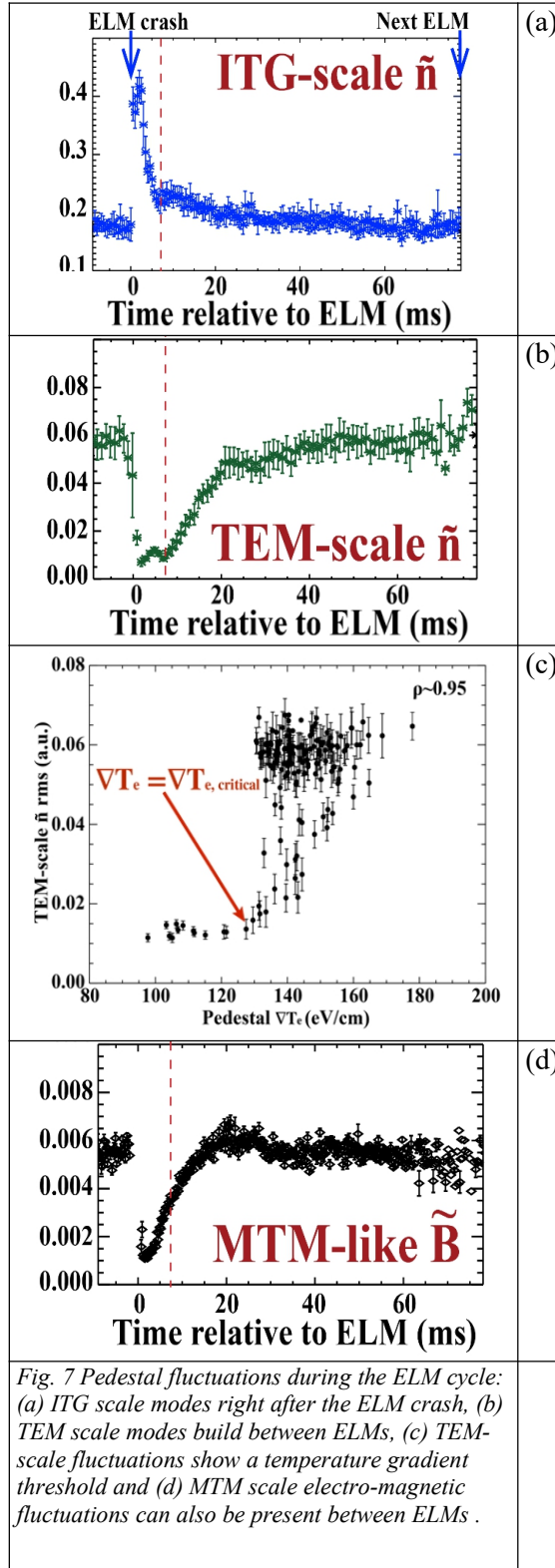
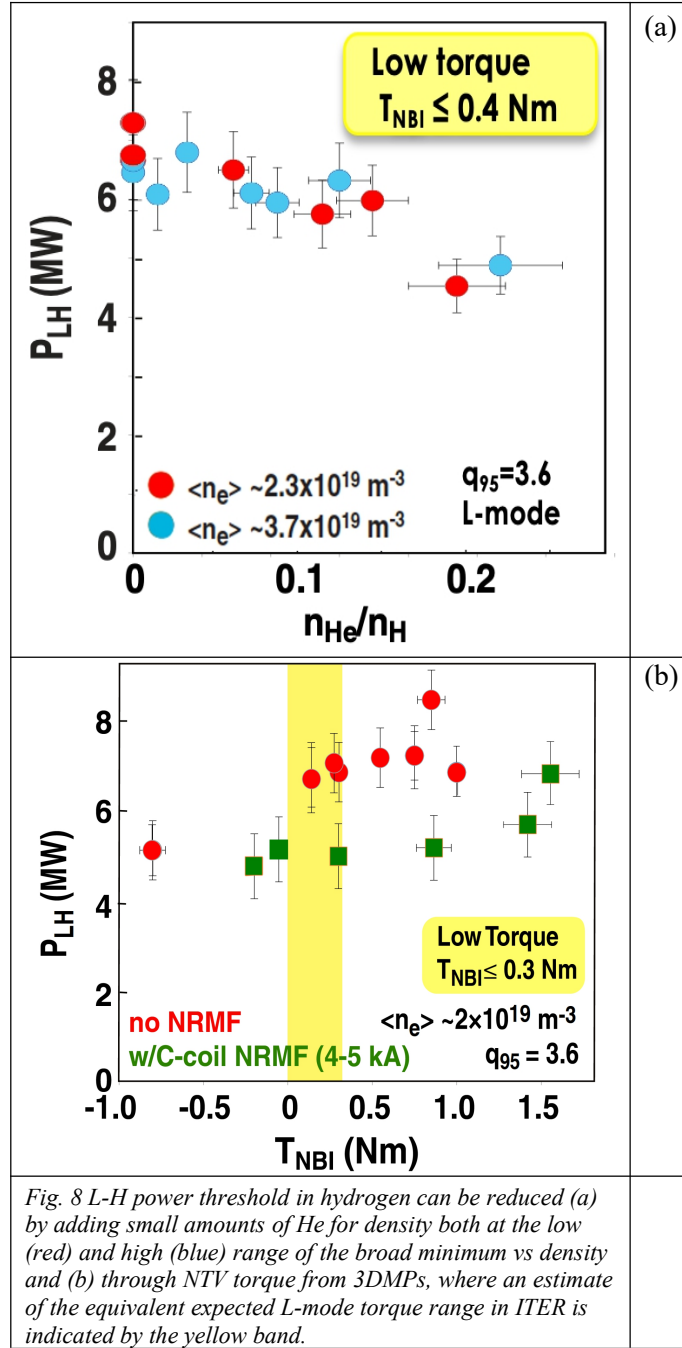
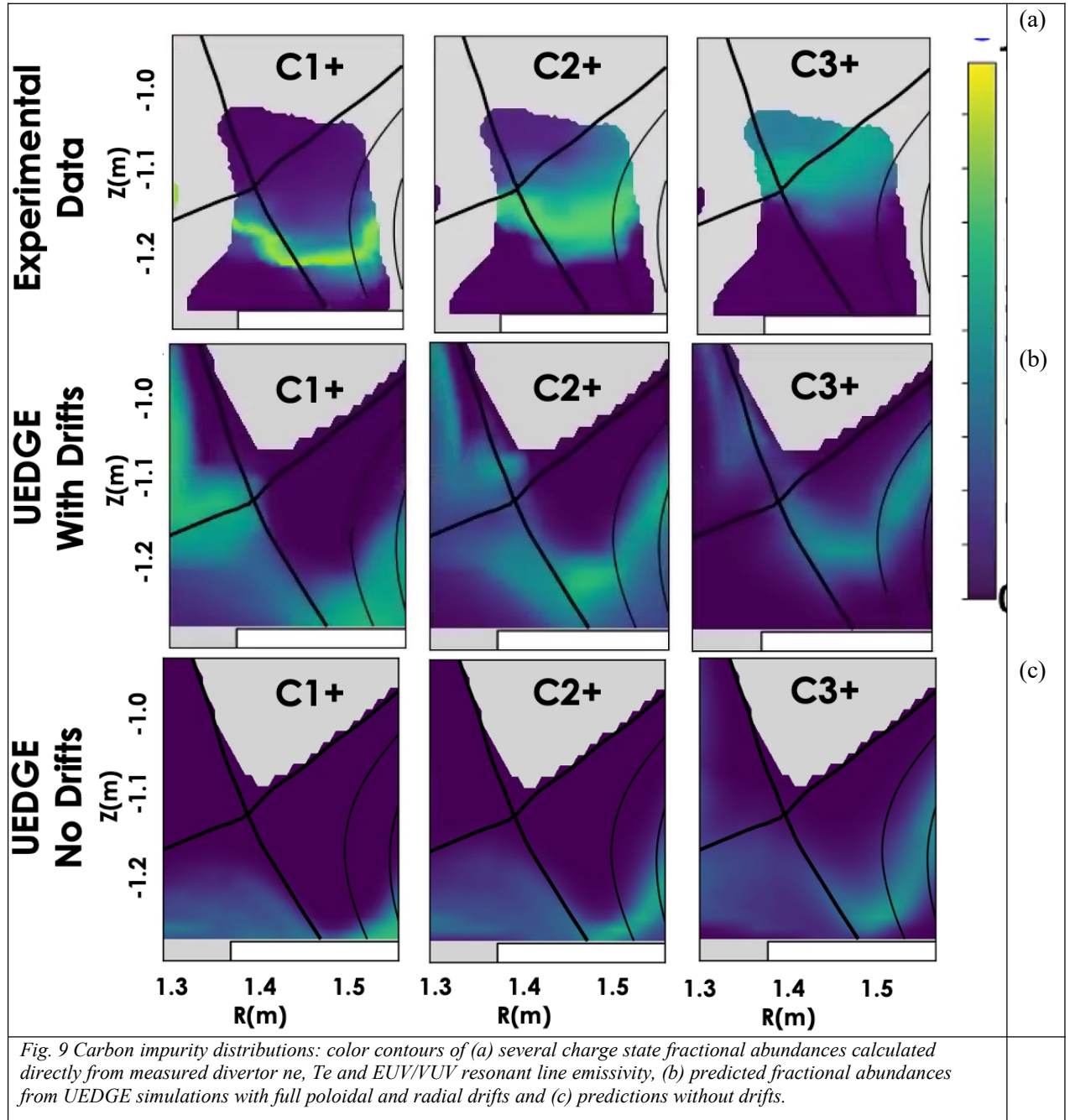
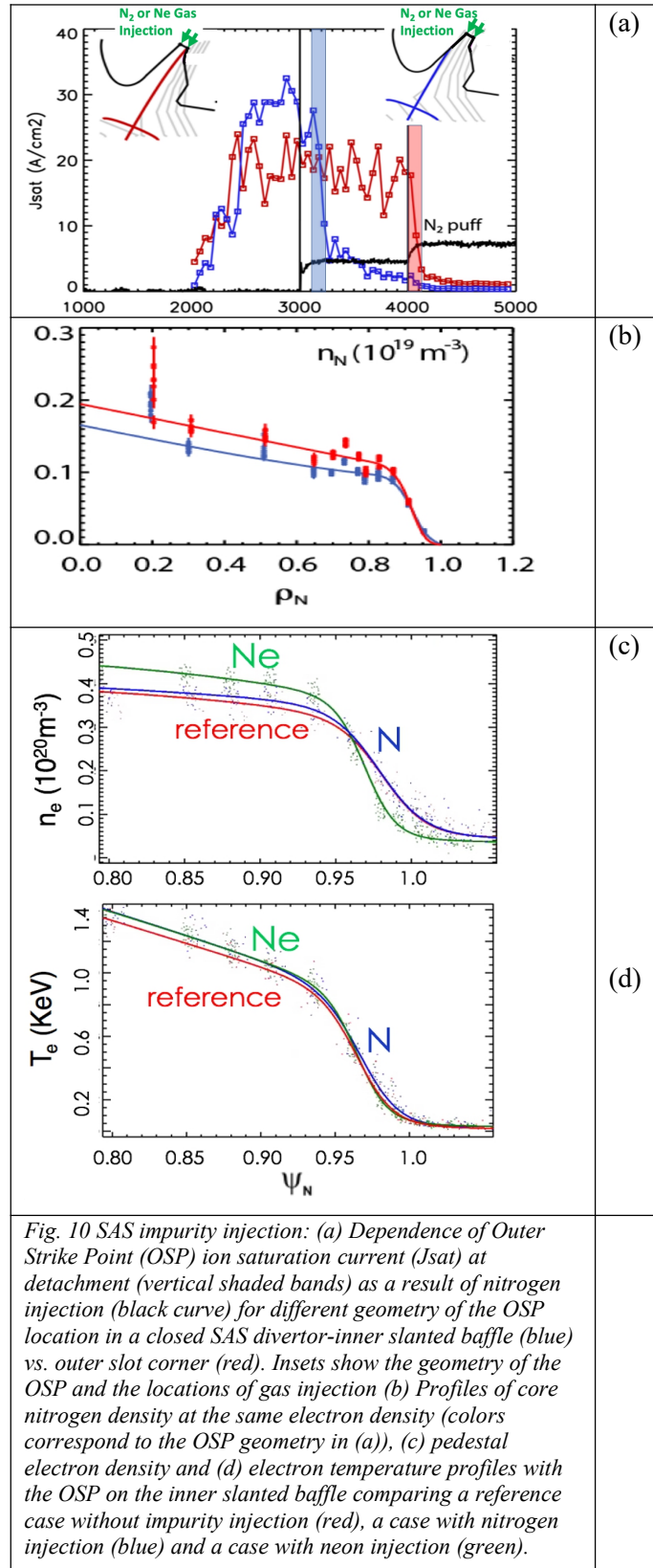


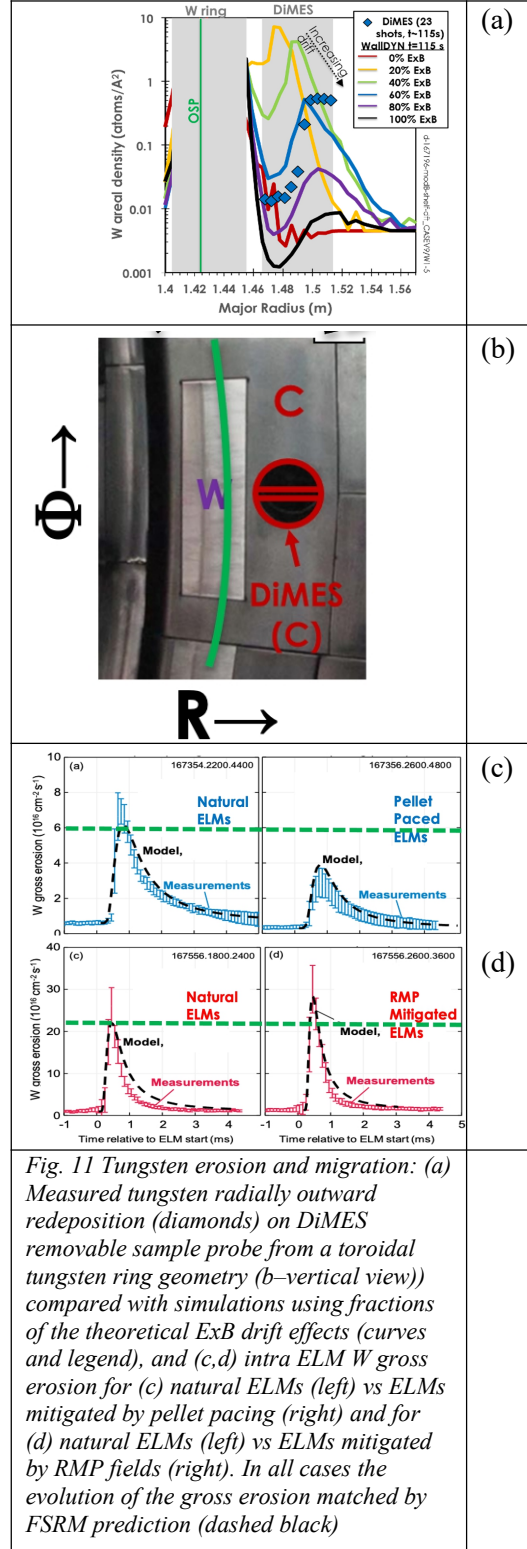
Fig.6 Operational  $q_{95}$  windows of ELM suppression: (a)  $n = 3$  RMP coil current and  $D_\alpha$  (upper) showing suppression in the yellow bands, and (b) pedestal electron pressure ( $p_e^{ped}$ ) from experiment (blue), EPED prediction (black) and TM1 prediction (red), (c) color contours of TM1 predicted reduction in pedestal pressure versus  $q_{95}$  and  $I_{RMP}$  for DIII-D and the experimental radial field used (horizontal dashed line), and TM1  $p_e^{ped}$  reduction predictions for ITER with (d)  $n=3$  RMP or (e)  $n=4$  RMP.













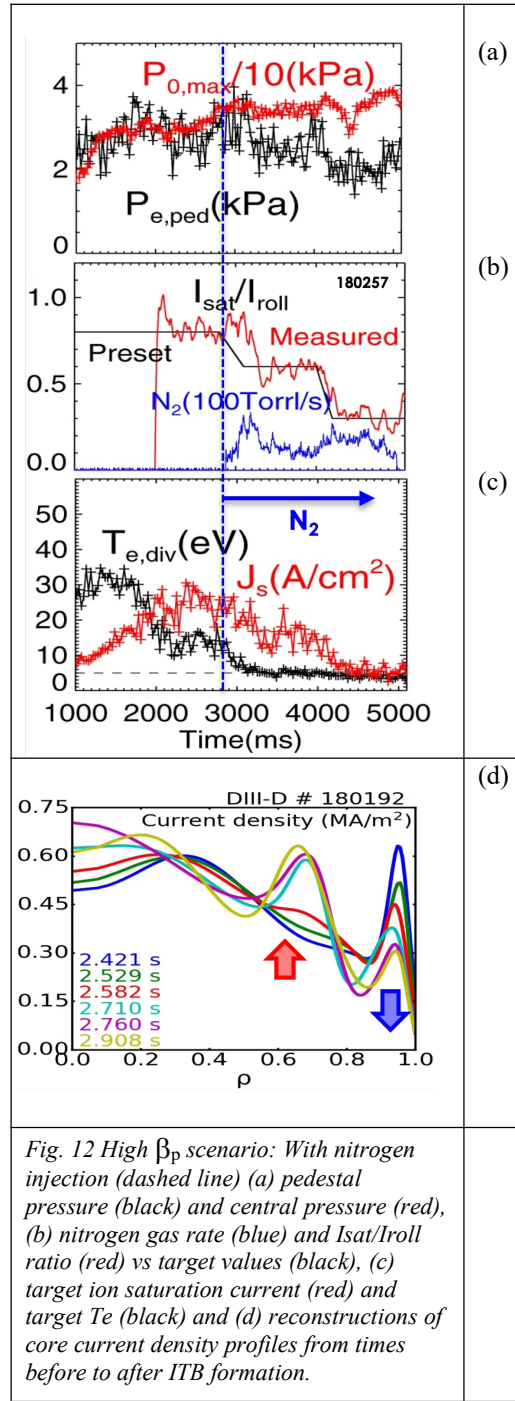


Fig. 12 High  $\beta_p$  scenario: With nitrogen injection (dashed line) (a) pedestal pressure (black) and central pressure (red), (b) nitrogen gas rate (blue) and  $I_{sat}/I_{roll}$  ratio (red) vs target values (black), (c) target ion saturation current (red) and target  $T_e$  (black) and (d) reconstructions of core current density profiles from times before to after ITB formation.

